



Fundamentals of MXene synthesis

Kang Rui Garrick Lim^{1,2,5}, Mikhail Shekhirev^{3,5}, Brian C. Wyatt^{4,5}, Babak Anasori⁴✉, Yury Gogotsi³✉ and Zhi Wei Seh²✉

Since the first report on $Ti_3C_2T_x$ in 2011, the family of two-dimensional transition metal carbides, nitrides, and carbonitrides (MXenes) has increased substantially to include single and multi-element MXenes, with many more yet to be synthesized but predicted to possess attractive properties. To synthesize these elusive MXenes as well as to improve and scale up the manufacturing of known MXenes, a deeper mechanistic understanding of their synthesis processes is necessary, from the precursors to the etching–exfoliation and final intercalation–delamination steps. Here we examine computational modelling and in situ and ex situ characterization data to rationalize the reactivity and selectivity of MXenes towards various common etching and delamination methods. We discuss the effects of MAX phases, the predominant precursor, and other non-MAX layered materials on MXene synthesis and their resultant properties. Finally, we summarize the parameters behind successful (and unsuccessful) etching and delamination protocols. By highlighting the factors behind each step, we hope to guide the future development of MXenes with improved quality, yield and tunable properties.

Since the first report of Ti_3C_2 in 2011¹, the family of two-dimensional (2D) transition metal carbides, nitrides, and carbonitrides (MXenes) has greatly expanded and made an impact in the fields of energy storage, electromagnetic interference shielding, optoelectronics, water desalination, catalysis, medicine, and many others^{2–4}. With their unique combination of properties, including high electrical conductivity (up to $24,000\text{ S cm}^{-1}$ for $Ti_3C_2T_x$)⁵, liquid-phase processability⁶, tunable surface functionality⁷ and outstanding mechanical properties (Young's modulus up to 386 GPa for $Nb_4C_3T_x$)⁸, MXenes have attracted great interest^{4,9}, generating thousands of publications in the past decade¹⁰.

MXenes have the general chemical formula $M_{n+1}X_nT_x$, and can be described as comprising $n + 1$ layers ($n = 1–4$) of one or more group 3–6 early transition metals ('M'), interleaved by n layers of carbon and/or nitrogen atoms ('X'), with T_x denoting surface terminations (for example, –F, –O, –OH) on the outermost exposed M layers^{11,12}. More specifically, the X element atoms in MXenes occupy the octahedral interstitial sites of M in their hexagonal crystal sublattice, which results in subunits of edge-sharing M_6X octahedra, while the surface groups occupy different sites of M, depending on the T_x and M chemistry¹³. MXenes are typically produced in three steps (Fig. 1). The first step is to synthesize layered MXene precursors, from which the crystal structure is derived; these are typically MAX- ($M_{n+1}AX_n$, where 'A' refers to group 11–16 atoms, such as Al, Si and Ga) or non-MAX-phase layered materials with more than one 'A' atomic layer (for example, $M_{n+1}A_2X_n$) or with carbide layers of A elements (for example, $M_nA_3X_{n+2}$). Second, the A atomic layers are etched away, exfoliating the precursors to produce weakly bonded MXene multilayers^{11,12}. During the A atomic layer etching process, the weaker M–A bonds (relative to the M–X bonds) are cleaved, resulting in undercoordinated M metallic surfaces that will be rapidly saturated again via reaction with T_x species from the etchant¹⁴. Third, the exfoliated multilayer MXene sheets are delaminated to yield single- to few-layer MXene sheets^{15,16}.

Both the chemical and structural complexities of synthesized MXenes have substantially increased over the past decade to encompass MXenes with two or more transition metals in ordered structures or disordered solid solutions^{17–19}. The variety, uniformity, and compositional control of T_x surface groups, which heavily influence the behaviour of MXenes, now extend beyond –O, –OH and –F to include other halogens (–Cl, –Br, –I), chalcogens (–S, –Se, –Te), imido (–NH) groups and termination-free (\square) MXene surfaces^{7,20}.

Although these developments have expanded the number of methods used to synthesize MXenes¹¹, most are heavily reliant on wet acid etching using hazardous solutions containing hydrofluoric acid (HF)²¹. Moreover, seven out of the top ten challenges for the upcoming decade ranked by MXene researchers in late 2020 were directly related to MXene synthesis⁴ (Supplementary Table 1), underscoring the need for a deeper mechanistic understanding to guide future synthetic efforts. The most pressing challenges include but are not limited to the production of large-area single-layer flakes²², chemically safe synthesis²³ and controllable surface chemistry⁷, which can be addressed through mechanistically driven synthesis development. With such a large compositional space and the potential for tunable material behaviour, a critical evaluation of current MXene synthetic techniques at every stage of the synthesis process, from precursors to single-flake MXenes, is necessary for future development of this growing family of materials. This Review aims to facilitate the theory and mechanistically guided design of new approaches to synthesize available MXenes and enable the synthesis of MXene structures and compositions with improved quality, yield and tunable properties.

In this Review we compare the different methods at each stage of the MXene synthesis process. We discuss the reaction pathways and the effects of composition (M, A and X) on MXene precursor synthesis and the resulting MXenes. Then, insights into the various etching processes during precursor exfoliation into multilayer MXenes (henceforth known as the etching–exfoliation process) are highlighted. We conclude by examining parameters that control the

¹Department of Chemistry and Chemical Biology, Harvard University, Cambridge, MA, USA. ²Institute of Materials Research and Engineering, Agency for Science, Technology and Research (A*STAR), Innovis, Singapore, Singapore. ³A. J. Drexel Nanomaterials Institute, and Department of Materials Science and Engineering, Drexel University, Philadelphia, PA, USA. ⁴Department of Mechanical and Energy Engineering and Integrated Nanosystems Development Institute, Purdue School of Engineering and Technology, Indiana University–Purdue University Indianapolis, Indianapolis, IN, USA. ⁵These authors contributed equally: Kang Rui Garrick Lim, Mikhail Shekhirev, Brian C. Wyatt. ✉e-mail: banasori@iupui.edu; gogotsi@drexel.edu; sehzw@imre.a-star.edu.sg

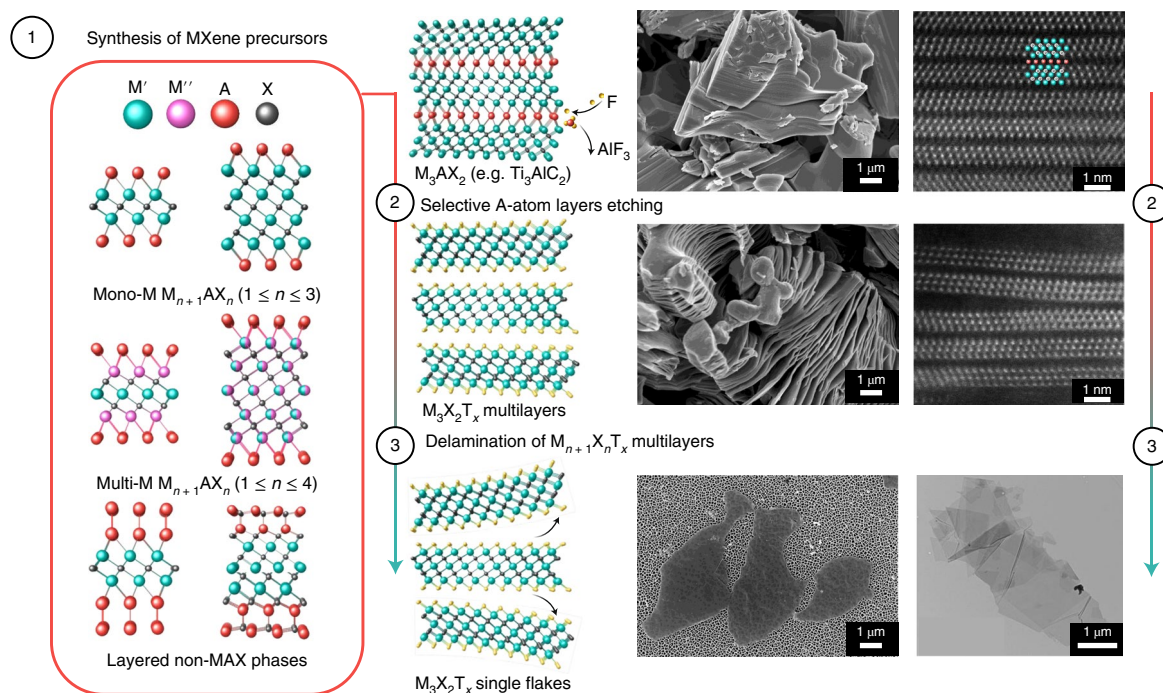


Fig. 1 | Synthesis of MXenes. Etching of the Ti_3AlC_2 MAX phase to produce $\text{Ti}_3\text{C}_2\text{T}_x$ MXene is used as an example. MXene synthesis starts with (1) synthesis of precursors such as MAX ($\text{M}_{n+1}\text{AX}_n$) and non-MAX (for example, $\text{M}_{n+1}\text{A}_2\text{X}_n$) phase layered materials. Non-MAX materials contain more than one layer of A atoms (such as $\text{Mo}_2\text{Ga}_2\text{C}$; ref. ³¹) or an aluminium carbide layer in between the MXene sheets (such as Al_4C_4 layers in between Hf_3C_2 MXene sheets in $\text{Hf}_3\text{Al}_4\text{C}_6$; ref. ³³). MAX phase materials can contain more than one M metal element (M' and M''), which can be structurally ordered (M' and M'' in distinct atomic layers) or form disordered solid solutions (M' and M'' randomly distributed in the metal layers). (2) MXene precursors are then etched to remove the A element layers and exfoliated to yield weakly bonded MXene multilayers that can be (3) delaminated to form single sheets. Yellow spheres represent T_x surface terminations. In the top and middle rows (Ti_3AlC_2 MAX (top); $\text{Ti}_3\text{C}_2\text{T}_x$ multilayers (middle)), scanning electron microscopy (SEM) images (left), and atomic-resolution cross-sectional scanning transmission electron microscopy (STEM) images (right) are shown. In the bottom row, ($\text{Ti}_3\text{C}_2\text{T}_x$ single flakes), a SEM image is shown on the left and a plane-view TEM image, instead of a STEM image, is shown on the right. SEM images adapted with permission from ref. ²¹, American Chemical Society. TEM images adapted with permission from ref. ⁸², American Chemical Society. STEM images adapted with permission from ref. ¹¹⁹ under a Creative Commons licence CC BY 4.0.

intercalation and delamination of multilayer MXene into single- to few-layer flakes (henceforth known as the intercalation–delamination process). In each section, we elucidate trends between methods to guide future synthetic efforts. Specifically, we combine theoretical modelling, as well as in situ and ex situ characterization data, to understand the mechanism behind the widely adopted precursor synthesis, etching–exfoliation and intercalation–delamination protocols. Although we focus on identifying common mechanistic trends among the various synthetic methods, we highlight a few complementary reviews with more details on specific MXene synthetic methods^{11,20,21,24}. We also centre our discussion around top–down synthetic methods and challenges in scalable MXene manufacturing. Top–down methods are the predominant means used to produce MXenes and are currently being evaluated for industrial-scale manufacturing^{22,25}. Readers are referred to seminal works on bottom–up MXene synthesis to learn more about atomic-scale growth mechanisms of 2D carbides^{12,26,27}.

Chemistry and synthesis of MXene precursors

Although bottom–up approaches have been used to synthesize MXenes^{12,26,27}, most MXenes are made via top–down methods and hence derive their structure and composition from their respective bulk layered carbide and nitride precursors³. Bulk transition metal carbides and nitrides possess a wide variety of chemical compositions and structures owing to their stability with M and X vacancies or mixed occupancies²⁸, which results in applications from catalysis²⁹ to use in extreme environments³⁰. Recently, the MXene

community turned to this historic wealth of studies on bulk transition metal carbides and nitrides to control the chemistry of precursor phases and synthesize MXenes with tunable and/or extreme properties^{2,13,31,32}. The MXene compositions synthesized so far have exploited the chemical diversity of layered transition metal carbides and nitrides, including both MAX and non-MAX phases, as MXene precursors^{1,33–36}. In this section we discuss the chemistry of these precursors and how their structure and stoichiometry affect the synthesis and properties of the resulting MXenes.

Precursor chemistry to predict exfoliation energy. Most experimentally realized MXenes are derived from bulk MAX phases that are structurally defined by M_{n+1}X_n layers interleaved by one (in MAX phases; Fig. 2a) layer of group 11–16 A-element atoms. In these precursors, the M_{n+1}X_n layers are held together by strong ionic/covalent M–X bonds within the layers and by weaker metallic M–A bonds between the layers (Fig. 2b). Similar M–X and M–A bonding exists in some non-MAX phases that have been exfoliated into MXenes, such as Mo_2CT_x from $\text{Mo}_2\text{Ga}_2\text{C}$ (Fig. 2c). These differences in bond strength allow exfoliation by cleaving the M–A bonds while maintaining the M_{n+1}X_n layers¹². To exfoliate the M_{n+1}X_n layers of MXene, the precursors are commonly placed into liquid acidic etchants²¹ or molten salts³⁷. The high stability of early transition metal carbides and nitrides in such environments^{38,39} allows M_{n+1}X_n layers to stay intact while M–A bonds are attacked by the etchant, leading to selective etching and removal of the A layers. One key factor for the successful isolation of M_{n+1}X_n MXene layers from

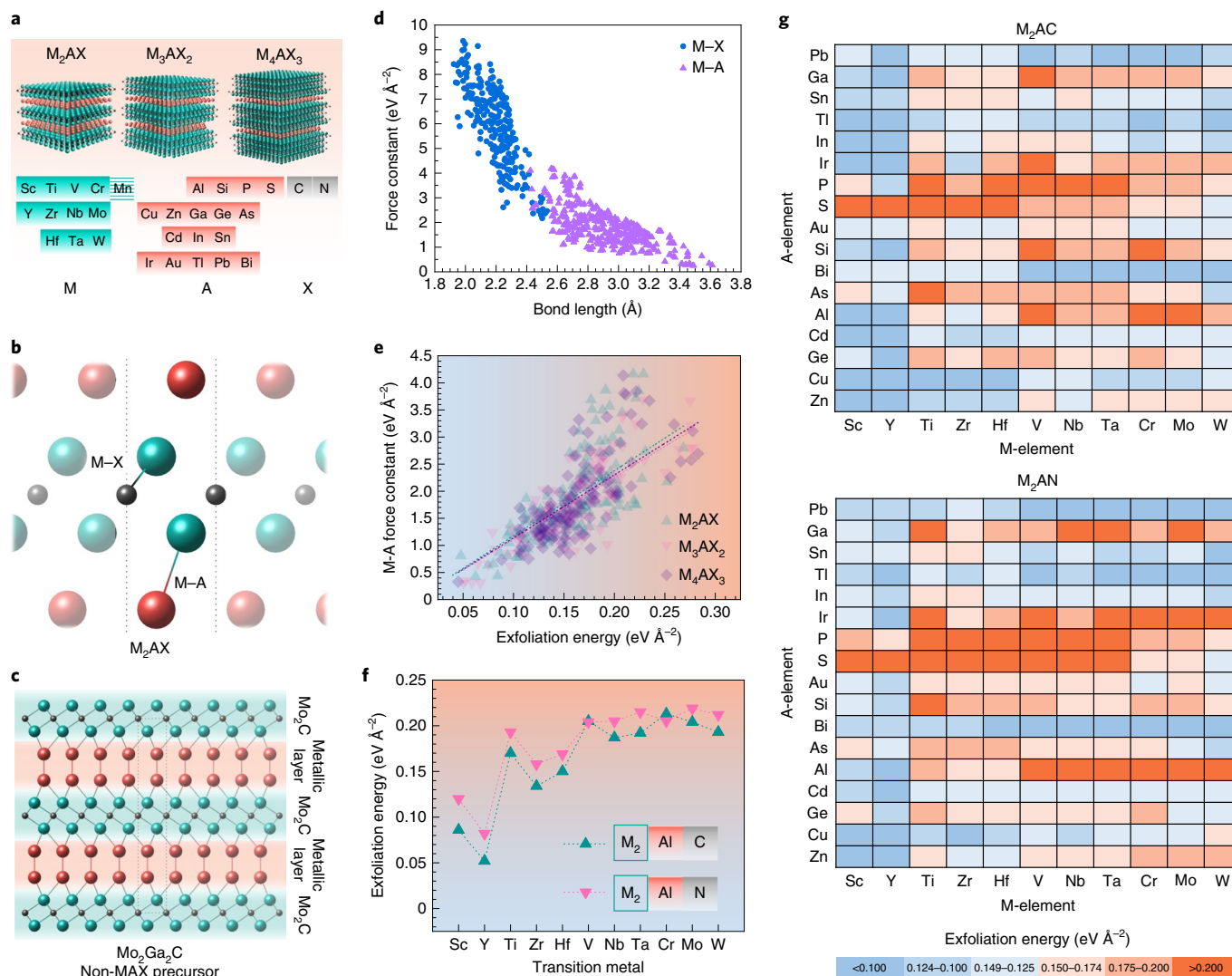


Fig. 2 | Relating the chemistry of mono-transition metal MXene precursor phases to their exfoliation energy. **a**, The diversity of MAX phases is shown through the possible M-A-X chemical compositions and the ability to form different n structures ($n=1-4$, M_5AX_n not shown). The bars on Mn indicate that Mn is the only M element shown here that exists in the MAX phase, but not in a pure MXene yet. **b**, Schematic of M-X and M-A bonds in a MAX phase, where M_2X layers are sandwiched between single A atomic layers. Blue, red and black spheres represent M, A and X, respectively. **c**, Bonding in Mo_2Ga_2C , a non-MAX phase precursor for Mo_2CT_x MXene. **d**, M-A and M-X bond lengths and bond force constants across common MAX phase compositions. **e**, The exfoliation energy of M_2AX , M_3AX_2 and M_4AX_3 MAX phases increases with higher M-A bond force constants. The dashed line is the regression line. **f**, Exfoliation energy of M_2AlX carbide and nitride MAX phases for different early transition metals M. **g**, Heat map of M_2AX MAX phase exfoliation energy across different M (horizontal), A (vertical) and X (top, bottom) compositions. Figure adapted with permission from: **d-g**, ref. ⁴⁰, Royal Society of Chemistry.

their bulk-phase precursors is the relative strengths of the chemical bonds present; more specifically, the strength of M-X compared with M-A bonds⁴⁰. The effect of these different bond strengths in MAX and non-MAX precursors can be seen in MAXenes production via mechanical exfoliation, as single-layer crystals of MAX and non-MAX phases have been isolated via shearing at the M-A interfaces⁴¹. Differences in composition (M, A and X) and bond chemistry also affect the structure, such as ordering in the M layers (for example, out-of-plane ordered compared with in-plane ordered MAX phases^{35,42,43}). We note that, from a practical point of view, other factors such as the choice of etchants and the synthetic procedures also affect the success of MAX to MXene production, because these factors determine the thermodynamic feasibility and kinetics of the etching reaction.

In general, the exfoliation energy of MAX and most non-MAX phases to MXenes is predicated on the relative strength of the M-X

(compared with the M-A) bond, which is approximated by bond force constants (Fig. 2d)⁴⁰. Poor exfoliation into MXenes occurs when both bonds are strong, and the MAX phase dissolves during etching if both bonds are weak⁴⁰. Specifically, precursor compositions with (1) particularly weak M-A bonds and (2) exceptionally strong M-X bonds possess lower exfoliation energy and hence are easily exfoliated into MXenes. Figure 2e illustrates trend (1) between the calculated exfoliation energy and M-A bond force constants^{40,44}. The investigated MAX phases were predicted with the same increasing exfoliation energy trend with stronger M-A force constants, irrespective of their MAX structure ($M_{n+1}AX_n$, $n=1-3$)⁴⁰. This result indicates that the MAX-to-MXene exfoliation energy depends less on the MAX structure (n value) and more on the surface transition metal M involved in both M-X and M-A bonding. The importance of the n value is discussed in the Etching and exfoliation mechanism section. The M-X bond strength, and hence the

exfoliation energy, also relies heavily on the chemical identity of X (X = C or N)—trend (2) in Fig. 2f. Using the M_2AlX MAX structure as an example, nitrides are predicted to have higher exfoliation energies than carbides with the same structure and M atoms (Fig. 2f)⁴⁰. This prediction corroborates with the experimental ease of exfoliating Ti_3AlC_2 (5% HF, 24 h)²¹ compared with the exfoliation of Ti_4AlN_3 (molten fluoride salts, 550 °C)⁴⁵. This difference was attributed to the weaker M–N (compared with M–C) bond strength arising from the additional valence electron in N (compared with C)^{13,40,46}—the additional electron places more nitride (compared with carbide) MAX candidates above the stability boundary of 3.6 to 4.5 electrons per atom⁴⁰. As a result, more nitride (compared with carbide) MAX phases are unstable, which could partially explain the current small number of nitride MXenes as compared to carbide MXenes^{2,47}.

MAX exfoliation also changes substantially across M–A compositions for both carbides and nitrides (Fig. 2g). M–A combinations with smaller M and/or A atoms, and/or a higher number of valence electrons, typically form stronger M–A bonds, leading to a smaller difference in the M–X and M–A bond energies⁴⁰. The effect of higher M atom valency predicts a lower exfoliation energy for Ti_3AlC_2 ($Ti = 3d^2$, $0.164 \text{ eV } \text{Å}^{-2}$) compared to a theoretical Mo_3AlC_2 MAX structure ($Mo = 4d^5$, $0.171 \text{ eV } \text{Å}^{-2}$)⁴⁰, and is reflected in the relative ease of exfoliating Ti_3AlC_2 (5% HF, 24 h, 23 °C)²¹ compared with Mo_2TiAlC_2 (50% HF, 48 h, 50 °C)⁴⁸. Similarly, the effect of higher valency and smaller atomic radii in the A elements is demonstrated when comparing the exfoliation energy of Ti_3AlC_2 ($Al = 143 \text{ pm}$ and $3p^1$, $0.164 \text{ eV } \text{Å}^{-2}$) to that of Ti_3SiC_2 ($Si = 111 \text{ pm}$ and $3p^2$, $0.186 \text{ eV } \text{Å}^{-2}$)⁴⁰, as seen in the harsher exfoliation conditions for Ti_3SiC_2 (30% HF + H_2O_2 , 45 h, 40 °C)⁴⁹ compared with Ti_3AlC_2 (5% HF, 24 h, 23 °C)²¹.

Compositional tuning of chemical bonding has also been exploited in non-MAX phases as an alternative to MAX phases, which have been experimentally difficult to exfoliate into MXenes. For example, it has not been possible to exfoliate the single Ga atomic layers from the Mo_2GaC MAX phase to synthesize Mo_2CT_x MXene. Instead, the non-MAX Mo_2Ga_2C layered phase with two atomic layers of Ga between Mo_2C layers (Fig. 2c) was synthesized and used to make Mo_2CT_x (refs. 50,51), relying on etching the weak Mo–Ga and Ga–Ga metallic bonds. Another example is the tricky synthesis of pure $Hf_3C_2T_x$ MXenes due to the poor phase purity of synthesized Hf_3AlC_2 MAX phases, because Hf_2AlC is often present in Hf_3AlC_2 MAX⁵². A creative solution uses the non-MAX $Hf_3Al_4C_6$ phase, which comprises covalently bonded Al_4C_4 layers interleaved between Hf_3C_2 layers³³. By introducing Si to create an $(Al, Si)_4C_4$ solid solution in the Al_4C_4 layers, the interfacial M–(Al, Si) bonding weakens to decrease their exfoliation energy towards $Hf_3C_2T_x$ MXenes³³. Thus, deliberate compositional design of non-MAX phases can yield MXenes that would otherwise be difficult to exfoliate via MAX phases.

In short, the difference between the ionic/covalent M–X bonds and the metallic M–A bonds lends a large degree of composition-based design for both MAX and non-MAX phases. Continued experimental exploration across different M–A–X chemical compositions, guided by their chemical bonding behaviour, will expand the variety of MXene precursors and hence MXenes.

Effect of precursor synthesis on the MXene structure. After considering the effects of chemical bonding in MAX and non-MAX structures on their exfoliation energy, the next step is to synthesize the MXene precursor. The top-down approach from precursor to MXene implies that the processing steps chosen to form the precursor MAX and non-MAX phases will substantially influence the subsequent MXene properties. Here we discuss the effect of elemental precursors (M, A and X) and the synthesis temperature of MAX phases on their properties and MAX phase purity.

Pressureless (atmospheric pressure) reactive sintering under an inert environment is commonly used to synthesize precursor phases (Fig. 3a). This technique creates porous sintered billets^{53,54} and facilitates their subsequent processing to powders for etching. Hot pressing and hot isostatic pressing have also been used, but the dense MAX phase bodies produced by these methods are more difficult to crush and mill into powders. Most MAX phases for MXene production have been formed using one of two powder mixture combinations: a pure elemental powder mixture of M, A and X (for example, Ti, Al and C for Ti_3AlC_2) or carbide/nitride powder mixtures of MX and/or AX, with additional elemental powders of M, A and X (for example, Ti, TiC and Al for Ti_3AlC_2)^{55,56}. Metal hydrides, especially titanium hydride, are also used⁵⁷. Additionally, MAX phase synthesis in the presence of molten salts, which can be further extended to MXene synthesis, is gaining momentum^{37,58}.

MAX-phase formation using these powder mixture combinations follows very distinct formation paths (Fig. 3b,c). Ex situ X-ray diffraction on an elemental powder mixture of Ta, Al and C revealed the intermediate compounds during the sintering process: mixed Ta–Al intermetallics with some TaC from 700 to 1,300 °C, ternary non-MAX Ta–Al–C carbides with some MAX (Ta_2AlC and Ta_4AlC_3) from 1,300 to 1,500 °C, followed by Ta_2AlC MAX and Ta_4AlC_3 MAX as the primary phases above 1,500 °C (ref. 53). This observation suggests that reactive sintering of elemental powder mixtures first forms intermetallic M–A compounds, after which these intermetallic compounds nucleate binary carbide layers on the carbon interface to form non-layered ternary M–A–X phases^{59–61}. Figure 3b depicts the proposed formation mechanism for Ti_3AlC_2 MAX. Conversely, MAX phase formation via carbides or nitrides as precursors follows a different formation path. In situ diffraction studies on Ti_3AlC_2 MAX formation from mixtures of TiC, ($0.5 < y < 1.0$) and Al reveal that, at ~700 °C, partial carbon-vacancy ordering in $TiC_{0.67}$, parallel to the (111) plane (note the similar close-packed nature of both the cubic TiC (111) and hexagonal Ti_3AlC_2 (0001) planes), permitted Al diffusion into $TiC_{0.67}$ to form Ti_3AlC_2 (ref. 62). Other studies also show that Ti_2AlC is converted to Ti_3AlC_2 in the presence of TiC_y ; carbon-vacancy ordered TiC_y in the form of Ti_2C layers combines to form higher-order layers of carbon-vacancy TiC_y in the form of Ti_3C_2 , while Al diffuses into the carbon-vacancy sites at temperatures above 1,400 °C (ref. 62). These studies suggest that the formation pathway using powdered carbide or nitride mixtures relies on carbon- or nitrogen-vacancy-assisted diffusion of M and/or A atoms into the structure to yield the eventual MAX phase (Fig. 3c).

The choice of starting precursor powders used to form the MAX phases, and their different formation pathways, has a pronounced effect on the MAX structure. Examples include defects, such as vacancies (M, A and/or X; Fig. 3d), at the atomic scale, and differences in the MAX grain sizes and shapes on the micro/macroscale (Fig. 3e, top row). These variations in the MAX structure and stoichiometry are consequently translated to the resulting MXene morphology and behaviour⁶¹. For example, the average flake sizes of $Ti_3C_2T_x$ MXene derived from Ti_3AlC_2 MAX produced at 1,650 °C using three different carbon sources (graphite, TiC and amorphous carbon lampblack) were 4.2 μm, 2.6 μm and 0.5 μm, respectively, with as-filtered film electrical conductivity values of $4,400 \pm 110 \text{ S cm}^{-1}$, $3,480 \pm 60 \text{ S cm}^{-1}$ and $1,020 \pm 50 \text{ S cm}^{-1}$, respectively (Fig. 3e, bottom row; $Ti_3C_2T_x$ from amorphous carbon lampblack is not shown)⁶¹. The larger flake sizes and higher electrical conductivity of $Ti_3C_2T_x$ derived from Ti_3AlC_2 via elemental powder mixtures using graphite (compared with amorphous carbon) as the carbon source suggest that the graphitic carbon layers acted as nucleation sites for Ti–Al intermetallics and/or elemental Ti layer growth towards larger Ti_3AlC_2 grain sizes⁶¹. The intermediate flake size and conductivity of $Ti_3C_2T_x$ derived from TiC-produced Ti_3AlC_2 could be due to the variable concentration of carbon vacancies (value of y in TiC_y)⁵⁵. The

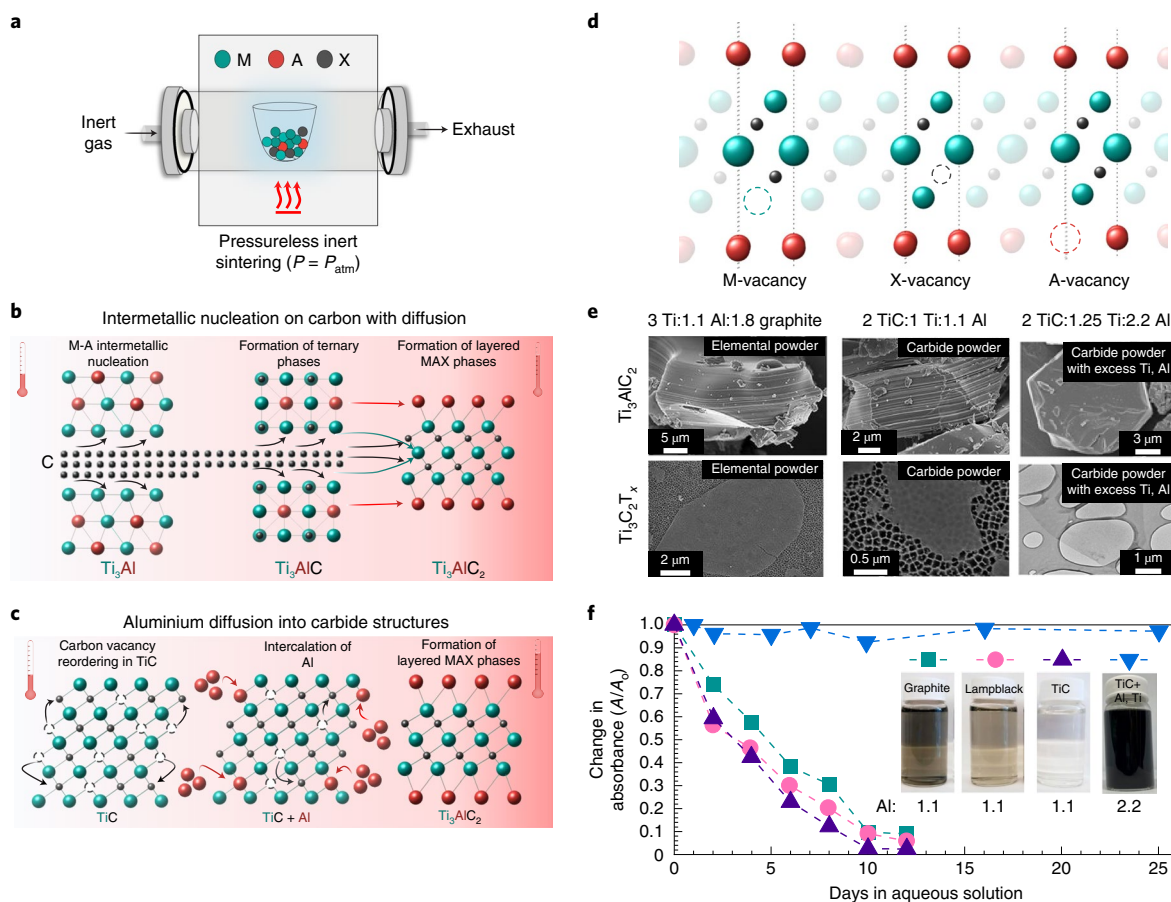


Fig. 3 | Effect of the MAX synthesis method on the mono-transition metal MXene produced. **a**, Synthesis of MAX, a common MXene precursor, typically begins by pressureless sintering in an inert atmosphere with a mixture of powdered M, A and X precursors. **b**, Using elemental powder precursors, synthesis of the Ti_3AlC_2 MAX phase begins with Ti-Al intermetallics formation, followed by carbon diffusion into the intermetallics to form Ti_3AlC_2 . **c**, Using carbide powder precursors, synthesis of the Ti_3AlC_2 MAX phase begins with diffusion of Al into the vacancies in the TiC structure to form Ti_3AlC_2 . **d**, Synthesis of MAX phases forms vacancies (M, A and/or X) in the structure. **e**, The choice of precursor powders has a distinct impact on the MAX grain size/shape and properties of the resultant MXene flakes. The images shown are SEM micrographs. From left to right: Ti_3AlC_2 MAX (top row) is produced by elemental powder (graphite), TiC carbide powder and TiC carbide powder with excess Ti and Al, respectively. Ti_3AlC_2 MAX produced using amorphous carbon lampblack (elemental carbon) is not shown. The bottom row shows $Ti_3C_2T_x$ MXene flakes derived from Ti_3AlC_2 MAX prepared using the respective methods above. **f**, Defects in the MAX structure are translated to their derivative MXenes, as seen in the difference in the aqueous oxidation stability of $Ti_3C_2T_x$ produced from Ti_3AlC_2 MAX prepared using different carbon precursors (graphite, amorphous carbon lampblack, TiC or TiC with excess Al and Ti, denoted as TiC + Al, Ti). Graphite and amorphous carbon lampblack are elemental carbon sources, and TiC is a carbide powder source. A decrease in absorbance indicates MXene oxidation and degradation. Absorbance values are normalized against initial absorbance values on day 0 (A_0). Digital images (inset) show $Ti_3C_2T_x$ MXene solutions prepared using the various Ti_3AlC_2 sources after 12 days. The number below the digital images indicates the ratio of Al added relative to the stoichiometric Al content in Ti_3AlC_2 . Figure adapted with permission from: **e** (right column), ref. ⁵⁵, American Chemical Society; **e** (left and middle columns), **f**, ref. ⁶¹, American Chemical Society.

lower conductivity of the $Ti_3C_2T_x$ MXene made from TiC-produced Ti_3AlC_2 also highlights the effect of the MAX-phase sintering temperature— $Ti_3C_2T_x$ prepared from TiC-produced Ti_3AlC_2 (2 TiC: 1 Al: 1 Ti) at a lower temperature of 1,400 °C exhibits much higher electrical conductivities, from 8,000 (ref. ⁶³) to 15,000 $S\ cm^{-1}$ (ref. ²²). The lower electrical conductivity of $Ti_3C_2T_x$ MXene made from the 1,650 °C-synthesized Ti_3AlC_2 can be attributed to defect formations (vacancies) or the lack of stoichiometric ratio in the elements (due to Ti and Al sublimation) during synthesis at higher temperatures.

Recently, Ti_3AlC_2 MAX was synthesized using TiC as the carbon source, but with excess Al and Ti (TiC:Al:Ti = 2:2.2:1.25 instead of the stoichiometric ratio of 2:1:1, rightmost column in Fig. 3e)⁵⁵; this afforded Ti_3AlC_2 MAX phases with detectable Ti-Al intermetallic impurities⁵⁵. After impurity removal and HF/HCl etching, the synthesized Ti_3AlC_2 MAX produced $Ti_3C_2T_x$ MXene with a modest 1.6- μm average flake size but a significantly improved electrical

conductivity of $\sim 20,000\ S\ cm^{-1}$. This improvement was attributed to an increase in carbon content to reach the stoichiometric Ti:C ratio in the Ti_3AlC_2 MAX phase⁵⁵, suggesting that an excess of metals may remove oxygen from the sintering environment and prevent loss of carbon, minimizing the vacancies (or substitutional oxygen) in the carbon sublattice. Additionally, the degradation rate of delaminated MXenes in aqueous colloidal solutions can qualitatively indicate defect concentration in the MAX phases used, because MXene oxidation is substantially enhanced by defects in the MXene structure⁶¹. Whereas $Ti_3C_2T_x$ MXene produced with stoichiometric ratios of Al and Ti with different carbon precursors (elemental sources such as graphite or amorphous carbon lampblack, or powdered carbide sources such as TiC) degraded significantly within a week⁶¹, $Ti_3C_2T_x$ MXene produced from TiC with excess Al and Ti demonstrated no detectable signs of oxidation as a dilute aqueous colloid over many months (Fig. 3f)⁵⁵.

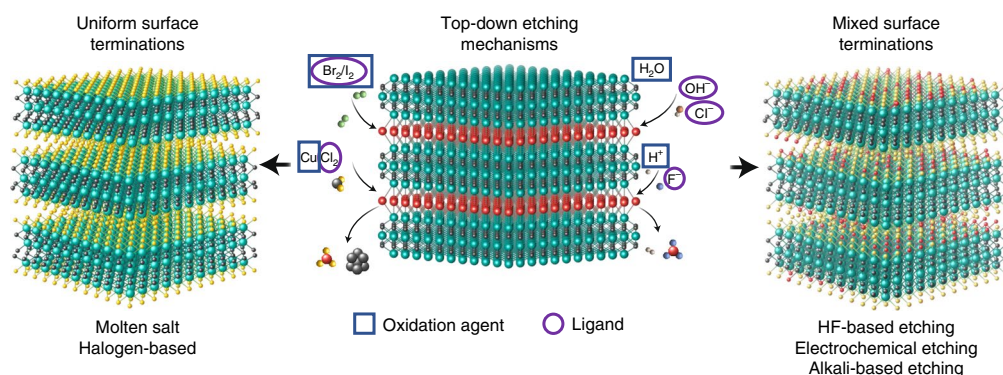


Fig. 4 | Top-down etching routes for MXene synthesis. Etching routes are categorized based on the uniformity of T_x surface terminations in the resultant MXene after etching. Molten salt and halogen-based etching processes yield MXenes with uniform surface terminations (left), whereas HF-, LiF/HCl-, NaOH/KOH-solution and electrochemical etching produce MXenes with mixed surface terminations (right). Regardless of the route, etching involves oxidizing the A element, most commonly Al, and binding the oxidized A product with a ligand, such as F^- or OH^- , to be transported as a soluble by-product away from the precursor to facilitate further etching. In the MAX (middle) and MXene (left and right) structures, cyan, red, grey and yellow spheres represent M, A, X and T_x , respectively.

To conclude, the M–A–X chemical composition can be used to predict the exfoliation energy of the MXene precursors. When synthesizing these MAX and non-MAX materials, the formation pathway, choice of elemental precursors, ratios of raw materials and the sintering conditions must be considered, because they all influence the properties of the precursor formed and, subsequently, the MXene. These considerations remain understudied in the broader MXene literature, particularly for MXenes other than $Ti_3C_2T_x$, even though they can strongly affect the properties of MXenes. Future studies should explore the effects of M, A and X composition and the formation pathways of MAX and non-MAX precursors.

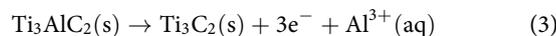
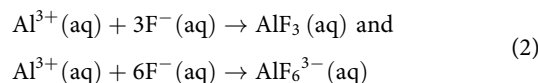
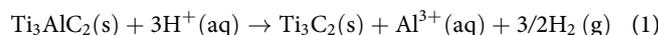
Mechanism of MXene synthesis

After formulating and synthesizing the MAX (and non-MAX) phase precursors, they are etched and then exfoliated to produce multilayer MXenes. In the first report¹, HF was used as an etchant to remove Al layers from Ti_3AlC_2 . Many more protocols have since been developed, ranging from direct and indirect HF-based syntheses to electrochemical, alkaline, molten salt and halogen etching^{11,64}. Weakly bound multilayer MXenes can be further delaminated into few- to single-layer 2D sheets¹². An atomistic understanding of MXene etching and delamination provides the first steps towards understanding why some methods only produce specific MXenes, and how the MXenes' properties and surface chemistry can be controlled through synthesis. In this section, we highlight trends and differences between the existing etching–exfoliation and intercalation–delamination methods, examining the selectivity of the different methods towards specific MXenes.

Etching approaches. In top-down MXene synthesis, the A atomic layer is selectively removed from the precursor, leaving the $M_{n+1}X_n$ layers intact (Fig. 4). The A element in MAX has a nominal oxidation state close to zero (for example, Al^0 in Ti_3AlC_2)⁴⁶, so the etching process is an oxidation of the A atom (for example, to Al^{3+} or Si^{4+}). Theoretically, the ability to remove the A element depends on the Gibbs free energy of the etching reaction, which, in the case of HF etching of Al-based MAX phases, is related to the bond strength of the M–A bond compared with that of the M–X bond, as well as other factors such as the Gibbs free energy of by-product formation. More generally, exfoliation also depends on the oxidation of the A element, and its subsequent conversion to soluble by-products via ligation, to be transported away from the precursor. The latter is crucial, as the etching process stops immediately if the oxidized products and/or the subsequent

hydrolysis products of the oxidized species (that is, aluminium oxides and hydroxides) restrict the etchant's access to the precursor reaction sites (subnanometre 2D galleries) for further etching⁶⁵. The etching solution should also be able to remove the protective native oxide layer⁶⁶, which is present on the surface of MAX-phase particles.

In the case of etching Al-based MAX phases (for example, Ti_3AlC_2) in HF-containing solutions (Fig. 4), protons (H^+) act as the oxidizing agent, and F^- serves as the ligand solubilizing the by-product (Al^{3+}), as shown in equations (1) and (2). Other oxidizer–ligand pairs can also be employed for the etching process. The F^- ligands can be replaced by OH^- because of the amphoteric nature of Al^{3+} , forming the basis for alkali-based etching routes⁶⁵, even though this route should be independently confirmed and further investigated. Oxidation of Al can also be performed electrochemically according to equation (3), which, when coupled with OH^- and/or Cl^- ligands, allows for fluoride-free electrochemical etching^{67,68}. Similarly, for non-Al-based MAX phases, the etchants must be able to perform oxidation and ligation of the A elements. For example, due to the strong Ti–Si bonding as previously discussed, etching Ti_3SiC_2 MAX requires an additional oxidizer(s), such as HNO_3 or H_2O_2 , alongside HF as the F^- ligand source⁴⁹:



Similar analyses can be applied to non-aqueous etching routes (Fig. 4). For halogen-based etching, the halogens and halide ions act as the oxidizing agent and ligand, respectively^{69,70}. In the molten salt route, the transition metal in the halide salt, such as Cu^{2+} in $CuCl_2$, serves as an oxidizing agent, while the halide ions act as ligands^{37,58}. Like fluoride ions in aqueous etching routes, halogen ligands play a crucial role in transporting the by-products of etching, such as $AlCl_3$, away from the etching sites via evaporation. The thermodynamic feasibility of molten salt synthesis was previously elucidated from the standard electrode redox potential standpoint³⁷. Recently, electrochemical oxidation of Al in molten salt systems was

reported⁷¹, where the applied positive potential is used for Al oxidation and Ti_3AlC_2 etching, as shown in equation (3).

Developing safe and environmentally friendly HF-free MXene synthetic routes is a critical challenge for MXene research⁴, and can be addressed by identifying appropriate HF-free oxidizer–ligand pairs as guided by redox potentials³⁷. Electrochemical etching of MXene precursors is very attractive due to the versatility of electrochemical set-ups, which can be applied in a variety of aqueous and non-aqueous systems, but their success has been limited thus far⁷¹. Additionally, little attention has been paid to etching MAX phases beyond Al-based ones. So far, there have been only a few examples of etching Si^{49} and $\text{Ga}^{50,51}$ for MXene production. Note that Ga was etched from a non-MAX $\text{Mo}_2\text{Ga}_2\text{C}$ structure. There are other MAX phases, for example Sn-based, that may offer M_{n+1}X_n chemistries that do not exist in the Al-based MAX family³⁶, and successful etching of these MAX phases may yield new MXene structures. Finding new oxidizer–ligand pairs and exploiting other unconventional approaches^{72,73} may lead to the discovery of MXene structures with unique properties.

In addition to the aforementioned solution-based etching routes, molten salt^{37,58} and halogen-based^{69,70} etching have gained popularity because they have produced MXenes with T_x functionalities (–Cl, –Br, –I, –NH, –S, –Se, –Te and \square) beyond those afforded by conventional HF-based etching⁷. We anticipate that these techniques will be adapted for the synthesis of MXenes beyond $\text{Ti}_3\text{C}_2\text{T}_x$, especially for nitride MXenes^{45,74,75}, which are challenging to prepare via HF etching³. Furthermore, molten salt synthesis is scalable and may offer an environmentally friendly approach for the one-pot synthesis of both MAX phases and their corresponding MXenes^{71,76–78}. Another advantage of these techniques is the realization of uniform T_x coverage, which can be substituted with many other surface groups⁷. These synthetic routes present an opportunity to investigate T_x -dependent MXene properties to develop T_x -engineered MXenes for surface chemistry-sensitive applications^{37,78}. However, delamination of MXenes produced by molten salt synthesis into single-layer flakes remains a challenge⁷⁹.

Regardless of the etching route (Fig. 4), the surface chemistry of MXenes is a key differentiator when compared to other 2D materials. It offers an additional approach, beyond structure and chemical composition, to tune MXene properties³. The ratio of the different surface T_x groups produced during etching depends substantially on both the etching conditions (for example, molten salt³⁷ or HF-based etching, with or without $\text{HCl}^{14,21}$, afford different surface terminations) and the chemistry of the MXene being etched (Ti-based MXenes have a higher affinity for –F terminations than Mo-based MXenes¹⁷). The surface terminations present on $\text{Ti}_3\text{C}_2\text{T}_x$ (O, F) are thermally stable up to 750–800 °C (refs. ^{80,81}), requiring relatively harsh conditions to remove or exchange the T_x groups. At the same time, covalent modification of the MXenes' surface using chemically reactive –OH (via condensation reactions)⁸², –F (via alkali treatment)⁸³ or –Cl and –Br groups (via substitution in a molten salt)⁷ has been used to tailor their properties.

Etching and exfoliation mechanism. Molecular dynamics simulation of Ti_3AlC_2 etching with HF reveals that the initial adsorption of H and F atoms on Ti atoms weakens the Ti–Al bond, ultimately removing Al as soluble AlF_3 and creating an interlayer space to facilitate further HF and H_2O intercalation for subsequent etching⁸⁴ (Fig. 5a). Notably, the resulting mixed surface terminations of $\text{Ti}_3\text{C}_2\text{F}_x(\text{OH})_{1-x}$ are random and non-uniform, corroborating the results of other computational studies for different MXenes (Ti_2N , Ti_4N_3 , Nb_2C , Nb_4C_3 , Ti_2C and Ti_3C_2)⁸⁵. This study suggests that the T_x distribution is largely independent of the MXene composition (M, X chemical identity) or the number of atomic layers (value of n)⁸⁵.

Unfortunately, designing in situ experiments to study the etching process is difficult because of the corrosive etchants used and

the gases released. Experimentally, several studies have attempted to deepen our understanding of the etching process step by step. The etching of Ti_3AlC_2 MAX with HF and LiF/HCl was probed ex situ by preparing cross-sections of Ti_3AlC_2 using focused ion beam (FIB), then exposing them to different etchants and obtaining TEM images at different stages of the etching process (Fig. 5b)⁸⁶. It was revealed that etching propagated stepwise, instead of simultaneously, in all MAX layers exposed to the etchant. The layers at the edge (surface) of the MAX particle were etched first, and the layers in the middle of the particle remained intact, despite contact with the etchant (Fig. 5c, right). A plausible explanation is the substantial strain induced by intercalation during etching and deformation in the etched $\text{Ti}_3\text{C}_2\text{T}_x$ MXene layers (Fig. 5c, left), which limits the number of MAX layers that can be etched simultaneously. In addition, pure HF etches through the grain boundaries, separating polycrystalline MAX particles into individual crystallites and thus completely etching the MAX particles. However, in situ generated HF from LiF/HCl does not attack the grain boundaries, leaving behind incompletely etched MAX, in the case of polycrystalline grains⁸⁶.

The etching of V_2AlC pillars deposited on a substrate was also investigated (Fig. 5d)⁸⁷. When defects were present, etching was initiated at the defect sites, propagating along crystallographic directions with a lower atomic density of Al (Fig. 5e)⁸⁷. Unexpectedly, at $\sim 45\ \mu\text{m}$ into the etched grain, the etching rate notably diminished, suggesting an upper size limit to the MAX particle that can be etched and, by extrapolation, the resulting MXene flake size. These studies^{86,87} demonstrate the vital role of defects (in the MAX phase), grain boundaries and particle size, and their influence on MXene etching.

These studies^{86,87} revealed another parameter affecting the experimental etching conditions—the thickness of the MXene layers (value of n in $\text{M}_{n+1}\text{X}_n\text{T}_x$). As discussed in the previous section, the strength of the M–A bond in carbide MAX phases determines the exfoliation energy within the same MXene structure (for example, M_3AlC_2 , $n = 2$). This correlation is clearly illustrated in the etching of Ti_3AlC_2 (5% HF, 24 h, 23 °C)²¹ compared with $\text{Mo}_2\text{TiAlC}_2$ (50% HF, 48 h, 50 °C)⁴⁸, due to the stronger Mo–Al bond compared with the Ti–Al bond. However, the thickness factor becomes apparent when comparing MXenes with similar chemistries. For example, $\text{Mo}_2\text{TiC}_2\text{T}_x$ ($n = 2$) and $\text{Mo}_2\text{Ti}_2\text{C}_3\text{T}_x$ ($n = 3$) require etching for 48 and 96 h in 50% HF, respectively⁴⁸. Both MXenes have Mo atoms occupying the outer layer¹⁷ and thus possess similar exfoliation energies based on the Mo–Al bonding. In another example, Nb_2CT_x ($n = 1$) and $\text{Nb}_4\text{C}_3\text{T}_x$ ($n = 3$) were produced by etching their corresponding MAX phases in 50% HF for 48 and 168 h, respectively⁴⁸. Finally, 10 h of etching was required for the synthesis of Ti_2CT_x ($n = 1$)⁵⁶ using 10% HF, compared to 18 or 24 h of etching for $\text{Ti}_3\text{C}_2\text{T}_x$ ($n = 2$)²¹ under similar conditions. The difference in etching conditions is possibly related to the stiffness of the M_{n+1}C_n layers, which increases with the n value⁶⁶. Deforming thicker MXene layers requires a larger force, and the mechanical stress limits intercalation of ions during the etching, thus demanding longer and/or harsher etching conditions for breaking the same M–A bonds.

We argue that the etching conditions discussed above are far from optimized. For example, the most common MAX phases, Ti_2AlC and Ti_3AlC_2 , which possess similar Ti–Al bonding but different n , are sometimes etched under similar conditions⁴⁸. Other parameters, such as the MAX synthesis method, particle size and the thickness of its protective oxide scale, can affect the experimental etching conditions and confound analysis. Systematic studies directed towards optimization of the etching conditions for different MXene chemistries are vital for improving our understanding of the fundamental mechanisms behind the etching process(es) and improving the quality, flake size and properties of MXenes. Furthermore, etching kinetics is an understudied area that can reveal more information about the etching mechanism for different MXenes. Studies of the

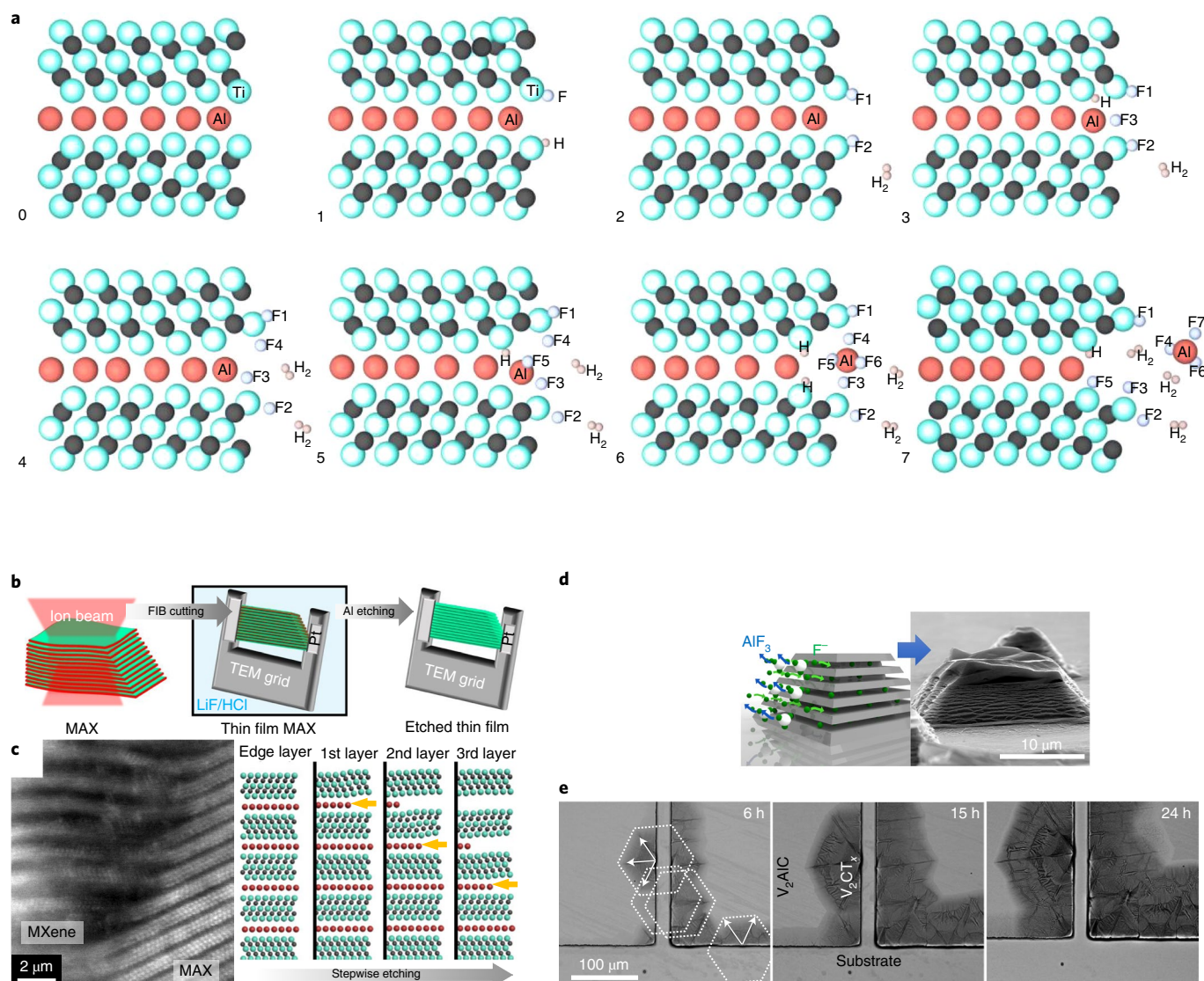


Fig. 5 | Mechanism of HF-based etching and exfoliation. **a**, Evolution of the lowest energy configuration of Ti_3AlC_2 MAX intercalated with 0-7 HF molecules, as indicated on the bottom left of each schematic. Atoms on the left edge are fixed. Adsorption of H and F atoms on Ti atoms weakens the Ti-Al bond to create an interlayer spacing to allow more HF and H_2O intercalation, eventually etching away the layer of Al atoms as soluble AlF_3 . **b**, Schematic of the study investigating the etching mechanism in Ti_3AlC_2 via TEM imaging at different stages of etching. **c**, Atomic-resolution STEM image of the etching boundary region (left) and schematic of the proposed etching process (right). Cyan, grey and red spheres represent Ti, C and Al atoms, respectively. This study illustrates a stepwise etching process: even as the Al atoms of all sheets are exposed to the etchant, etching occurs sequentially, starting from the surface, instead of all sheets being etched simultaneously. **d**, Schematic of the study investigating the etching mechanism in V_2AlC pillars via SEM imaging at different stages of etching. White and green spheres represent Al and F atoms, respectively. **e**, Top-down SEM images of V_2AlC pillars as a function of HF etching time (6, 15 and 24 h, from left to right). When defects are present, they initiate the etching process, which propagates in specific crystallographic directions. Dark areas indicate regions where Al was etched away and V_2CT_x was formed. Arrows show the preferred etching directions with a hexagonal-like pattern (white outline). Figure adapted with permission from: **a**, ref. ⁸⁴, American Chemical Society; **b,c**, ref. ⁸⁶, American Chemical Society; **d,e**, ref. ⁸⁷ Royal Society of Chemistry.

kinetics of Al extraction from Ti_3AlC_2 MAX are limited⁸⁸, necessitating further investigations.

Intercalation and delamination mechanism. Although multilayer MXenes obtained immediately from etching can be used for applications in adsorption and a few other fields⁸⁹, separating (delaminating) MXenes into individual 2D sheets is required for many other applications³. Separating MXene layers requires overcoming attractive forces between MXene layers (Fig. 6a). Higher adhesion energy values were measured for the thicker $\text{Ti}_3\text{C}_2\text{T}_x$ MXene ($n=2$), compared to monolayer graphene or thinner MXenes (Ti_2CT_x and

Nb_2CT_x)^{90,91}, due to the stronger dipole moment and higher polarity of $\text{Ti}_3\text{C}_2\text{T}_x$ (Fig. 6b). Hydrogen bonding between MXene layers and incomplete etching⁸⁶ further complicate the delamination process, rendering the mechanical exfoliation of MXenes somewhat challenging, at least for manufacturing few-layer flakes. Instead, intercalation of different molecules and ions, followed by agitation or sonication, is widely used (Fig. 6c)^{15,16}. Intercalants expand the interlayer space and weaken interflake interactions. Intercalants used for MXene delamination include solvents, organic molecules and ions¹². Subsequently, agitation and/or sonication (in a suitable solvent) provides the necessary energy to separate the weakly bound

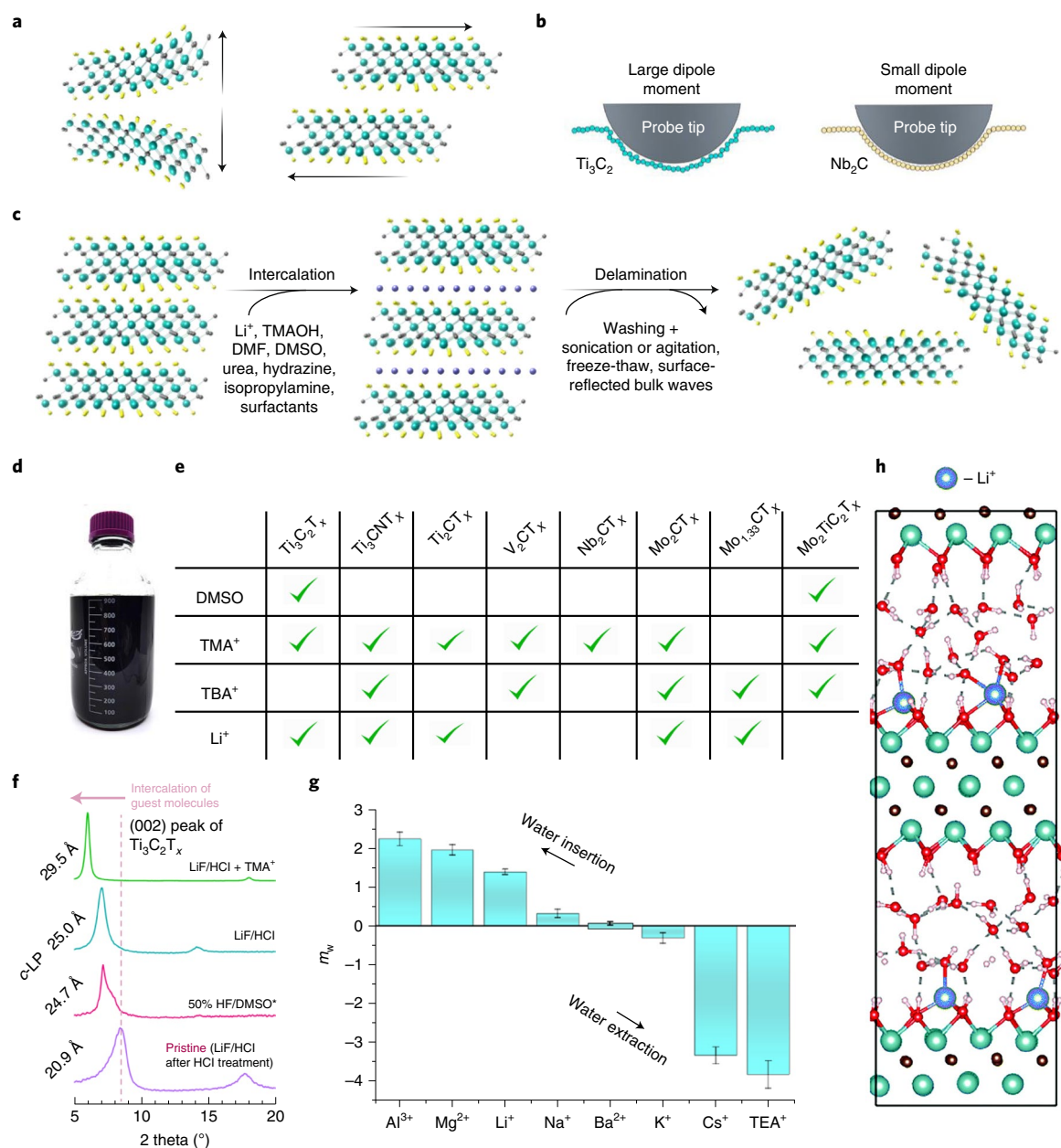


Fig. 6 | Intercalation-delamination mechanisms. **a**, Separation and delamination of two MXene layers is achieved either by overcoming adhesion forces between them by intercalation (left) or by shearing (right). **b**, Schematic comparing the contact friction for $\text{Ti}_3\text{C}_2\text{T}_x$ and Nb_2CT_x . The surface dipole moment density is higher and less uniform for $\text{Ti}_3\text{C}_2\text{T}_x$, resulting in higher friction and adhesion in $\text{Ti}_3\text{C}_2\text{T}_x$. **c**, Intercalation-delamination approach used for producing single-layer MXenes. Various molecules and ions can be intercalated between the layers. After washing and mechanical agitation (or sonication), MXene flakes separate and form stable colloidal solutions of single- to few-layer flakes. Cyan, grey, yellow and blue spheres represent M, X, T_x and intercalants, respectively. DMF, dimethylformamide. **d**, Digital photograph of a 1-l bottle of delaminated $\text{Ti}_3\text{C}_2\text{T}_x$ colloidal solution (10 mg ml^{-1}). **e**, Successful delamination intercalants reported for selected HF-etched (direct and indirect) MXenes: Ti_3C_2 with DMSO (ref. ¹⁵), TMA⁺ (ref. ²¹), Li⁺ (ref. ⁴⁸); Ti_3CN with TMA⁺ (ref. ¹²⁰), TBA⁺ (ref. ¹⁶), Li⁺ (ref. ⁴⁸); Ti_2C with TMA⁺ (ref. ¹²¹), Li⁺ (ref. ¹²¹); V_2C with TMA⁺ (ref. ^{48,121}), TBA⁺ (ref. ¹⁶); Nb_2C with TMA⁺ (ref. ^{48,121}); Mo_2C with TMA⁺ (ref. ¹²¹), TBA⁺ (ref. ⁵¹), Li⁺ (ref. ⁵¹); $\text{Mo}_{1.33}\text{C}$ with TBA⁺ (ref. ³⁴), Li⁺ (ref. ³⁴); Mo_2TiC_2 with DMSO (ref. ¹⁷), TMA⁺ (ref. ^{48,121}), TBA⁺ (ref. ¹²²). TMA⁺ and TBA⁺ refers to tetramethylammonium and tetrabutylammonium cations, respectively. DMSO, TMA⁺ and TBA⁺ intercalants are typically used for HF-etched MXene particles, and Li⁺ can be employed through LiF/HCl or HF/HCl etching, followed by LiCl delamination. **f**, X-ray diffractograms of $\text{Ti}_3\text{C}_2\text{T}_x$ films intercalated with different ions. The pristine $\text{Ti}_3\text{C}_2\text{T}_x$ film (purple curve) was prepared by HCl treatment of LiF/HCl-etched $\text{Ti}_3\text{C}_2\text{T}_x$ to remove interlayer Li⁺ via exchange with protons. Other $\text{Ti}_3\text{C}_2\text{T}_x$ films were intercalated with DMSO (red curve), hydrated Li⁺ (blue curve) and TMA⁺ ions (green curve). **g**, Experimental measurement of the number of water molecules per cation (m_w) inserted into, or extracted from, the $\text{Ti}_3\text{C}_2\text{T}_x$ electrode during intercalation. TEA⁺ refers to tetraethylammonium cations. **h**, Molecular dynamics simulation of the Li⁺ ion distribution in the $\text{Ti}_3\text{C}_2\text{T}_x$ MXene interlayer space, demonstrating strong interaction between Li⁺ and the $\text{Ti}_3\text{C}_2\text{T}_x$ surface. Blue, cyan, brown, red and white spheres represent Li⁺, Ti, C, O and H, respectively. Figure adapted with permission from: **b**, ref. ⁹¹, Elsevier; **d**, ref. ²⁵, Wiley; **e, f**, ref. ⁶⁶, American Chemical Society; **h**, ref. ¹⁰⁰, Royal Society of Chemistry. Panel **g** reproduced with permission from ref. ⁹⁹, American Chemical Society.

multilayers into a stable colloidal solution of single- to few-layered MXenes to achieve successful delamination (Fig. 6d)⁶⁶. The solvent choice depends on the MXenes' surface chemistry: polar solvents⁹² such as water, dimethylsulfoxide (DMSO), dimethylformamide (DMF) and *N*-methyl-2-pyrrolidone (NMP) are suitable solvents for O-, OH- and F-terminated MXenes^{82,93}.

Typical delamination agents that have been successfully used for selected MXenes are summarized in Fig. 6e⁶⁶. Many of these agents have been used previously for delaminating other layered materials, such as clays, oxides or MoS₂, into 2D sheets. DMSO was one of the first molecules used to intercalate and delaminate HF-etched Ti₃C₂T_x (ref. 93). For MXenes beyond Ti₃C₂T_x (ref. 48), tetraalkylammonium hydroxide bases, such as tetramethylammonium hydroxide (TMAOH) and tetrabutylammonium hydroxide (TBAOH), are effective delamination agents¹⁶. For Ti₃C₂T_x and other Ti-based MXenes (Ti₃CT_x and Ti-based solid solutions) prepared in the presence of HCl and fluoride ions, Li⁺ ions have been used for delamination²¹. Interestingly, Ti₃C₂T_x prepared via pure HF etching, and many other MXenes, cannot be delaminated with LiCl (Fig. 6e)⁹⁴. The delamination selectivity of LiCl was attributed to the -Cl terminations and/or Cl⁻ ions adsorbed on the MXene edges^{94,95}, and non-accessible interlayer spacing for ion exchange for MXenes etched with pure HF⁹⁶, illustrating the implication of the etching method for the delamination process. Considering the poor stability of MXenes in high-pH solutions (that is, TMAOH or TBAOH)⁹⁷ and the detrimental effect of bulky tetraalkylammonium ions on film conductivity^{48,98}, developing new delamination techniques with inorganic intercalants is a promising research direction.

In these intercalation–delamination approaches, the intercalation of ions and molecules results in a pronounced increase in the *c* lattice parameter of the multilayer MXenes (Fig. 6f). The MXene *c* lattice parameter includes two interlayer spacings and is derived from the MAX unit cell, which includes two MXene layers. Beyond ion intercalation, swelling of MXenes through water intercalation²¹ is also an essential step in aqueous delamination processes. For example, the intercalation of highly hygroscopic Li⁺ ions leads to substantial water insertion into the MXene interlayer spaces (Fig. 6g)⁹⁹. Moreover, Li⁺ ions interact strongly with the MXene surface (Fig. 6h)¹⁰⁰, which is another factor behind the successful delamination of Ti₃C₂T_x with LiCl. As a consequence of the intercalants persisting on the MXene layers even after delamination and extensive washing⁹⁸, these intercalants play a pivotal role in the colloidal stability of MXene flakes after delamination¹⁰¹. The addition of multivalent ions¹⁰² or the removal of adsorbed ions via acid treatments¹⁰³, which result in MXene flocculation and gelation, illustrate this effect. Taken altogether, these considerations complicate the development of new delamination approaches because they rely on fine-tuning the intercalant–surface interactions (which depend on the surface terminations and, thus, the MXene etching protocol) and intercalant–solvent interactions. Recent works on osmotic swelling⁹⁶ can provide the potential for delaminating MXenes beyond Ti₃C₂T_x using inorganic intercalants. More studies should be dedicated to delaminating Ti₃C₂T_x prepared via molten salt etching, which has proved to be challenging⁷¹ as current protocols involve dangerous chemicals⁷ and/or extended sonication⁷⁹ with limited yield.

Outlook

With an ever-expanding MXene family (approximately 50 presently reported), the level of chemical and structural complexity has far exceeded that of Ti₃C₂T_x to include one or more M elements^{3,12} with varying T_x surface groups^{7,20}. This expansion in the MXene family has been accompanied by new synthetic methodologies to meet the increasing demand for advanced in-plane, out-of-plane ordered, solid-solution and high-entropy MXenes³. In this regard, we stress the importance of understanding each step of the MXene synthesis process (precursor synthesis, etching and exfoliation, and

intercalation and delamination) for application-driven design. Each application demands a different set of properties (for example, lateral flake size, defects density and surface functionality). These properties are summarized in Table 1 for some representative applications, together with the known and possible synthetic routes towards MXenes with these qualities. A flowchart outlining the variety of physical and chemical properties of MXenes produced by the different MXene synthesis methods is provided in Supplementary Fig. 1.

For instance, MXenes are typically processed as slurries, also known as MXene clay¹⁰⁴ (partially delaminated multilayers with intercalated ions and water), inks¹⁰⁵ (colloidal dispersions of single- to few-layer flakes), and films¹⁰⁶ (vacuum-filtered, spin-, spray- or blade-coated restacked layers) for energy storage and photo-/ electrocatalysis⁹. In these two applications of MXenes as electrodes and catalysts, MXenes should possess (1) high electrical conductivity to reduce interfacial charge transfer resistance, (2) high aqueous solution processibility, hydrophilicity and electrochemical stability in aqueous electrolytes, and (3) T_x compositional control and tunability for optimal binding towards analytes⁹. Thus, aqueous HF¹⁰⁵, alkali⁶⁵ and halogen-based^{69,70} etchings are suitable methods to achieve T_x compositional control, while Lewis acid molten salt etchings can provide new T_x functionalities^{7,37,58} for specific binding to analytes to enable highly selective chemical transformations. Electrochemical etching of MAX electrodes provides an additional advantage by conveniently and directly producing MXene electrodes without additional transfer or electrode preparation steps⁷¹.

In another example, fundamental 2D transport phenomena studies, such as superconductivity, quantum transport and facet-dependent catalysis demand a higher degree of control over the thickness and defect concentration to minimize confounding factors. One approach is via physical or chemical vapour deposition growth of MXenes to produce large-area ultra-thin MXene sheets with controlled thickness and defect density^{12,26,27}. Recent progress in top-down processes enables the minimization of defects concentration⁵⁵ and the scalable production of monolayer Ti₃C₂T_x flakes with large lateral sizes (>10 μm)²². In all, identification of the key desired (and undesired) qualities for the intended application(s) is critical, and MXene synthesis can be suitably tailored towards material performance and selectivity.

To further expand the chemical and structural variety of the MXene family, we encourage investigations into the large family of both MAX (~155 known compositions)³⁶ and non-MAX layered carbides and nitrides. Specifically, future studies should focus on the effects of the M, A and X constituents and the various reaction pathways towards the synthesis of layered precursors, relating them to the resultant MXene morphology, structure and chemistry (for example, flake size, defects in the M and/or X sublattice, M and X elemental composition). For example, alloying the A atomic layers (forming solid solutions) or creating defects (vacancies) in those layers can weaken the alloyed M–A bond³³. Additionally, recent advances in the production of MAX phases with A elements beyond groups 13–16 of the periodic table (such as Fe, Co, Ni or Mn¹⁰⁷) present an attractive opportunity to synthesize MXenes from these new MAX phases. We speculate that molten salt synthesis may be applicable in this endeavour, given that they have been used to produce Ti₃C₂T_x from Ti₃ZnC₂ (A = Zn)³⁷. Etching of MAX phases with late transition metals as the A elements should also account for the increased valence electron count in these A elements. Future synthesis of new precursor non-MAX phases without M–A bonding can also focus on developing nanolamellar transition metal carbide or nitride structures with highly directional M–X bonding strengths, such as the in-plane Hf–C compared with out-of-plane Hf–C–(Al,Si) bond to produce Hf₃C₂T_x from Hf₃(Al,Si)₄C₆, which allows the possibility of exfoliation to MXene³³. Furthermore, an emerging subfamily of MXenes with X = B (MBenes)¹⁰⁸ brings new challenges in selective etching owing to the lower valence electron count of

Table 1 | Synthetic methods to produce MXenes for various applications

| MXene application | Desired physical properties | Known synthetic methods | Other possible synthetic methods |
|--|---|---|--|
| Energy storage and catalytic conversion Catalytic electrodes (electro-, photo-, photoelectrocatalysis) Batteries and supercapacitors | High electrical conductivity Tunable T_x towards selective adsorption of analyte Hydrophilicity and solution processability | HF etching ¹¹³ Electrochemical etching ⁶⁸ Alkali etching ⁶⁵ Halogen etching ⁷⁰ Lewis acid molten salt etching ³⁷ | None—most MXene synthesis methods today have already been evaluated for energy storage and conversion applications |
| Electromagnetic and electronic EMI shielding, antenna Electronics (MXetronics), optoelectronics, photonics, bioelectronics (MXtrodres) Wearable electronic sensors | High electrical conductivity Large surface area High mechanical stability Hydrophilicity and solution processability (for MXtrodres) | HF etching ¹¹⁴ | Alkali etching Halogen etching |
| Environmental and sensing Chemical (gas, liquid) Trace heavy metal adsorption Membranes (gas, liquid separation) | High electrical conductivity Hydrophilicity and solution processability Tunable T_x towards selective adsorption of analyte | HF etching ¹¹⁵ | Electrochemical etching Alkali etching Halogen etching |
| Biomedical Antimicrobial, antibacterial Biosensors, cancer theranostics Drug delivery Adsorption | Hydrophilicity and solution processability Tunable T_x towards selective adsorption of analyte Large surface area | HF etching ¹¹⁶ Electrochemical etching ¹¹⁷ Alkali etching ¹¹⁸ | Halogen etching |
| Mechanical Tribology (stiffness, adhesion, lubrication) Structural composites | Tunable T_x towards varying lubrication or stiffness Controllable MXene thickness Minimal defects Large surface area | HF etching ¹³ | Alkali etching Halogen etching Lewis acid molten salt etching |
| Fundamental studies 2D transport properties Facet, thickness-dependent properties (catalytic, optical, magnetic, electronic) | Controllable MXene thickness Minimal defects Uniform T_x Very large surface area | CVD growth of MXenes ²⁶ Lewis acid molten salt etching ⁷ | HF etching |

The most important physical and chemical properties of MXenes required for respective applications are also listed. CVD, chemical vapour deposition; EMI, electromagnetic interference.

boron in comparison to the carbon or nitrogen counterparts. These efforts in M, A and X compositions and non-MAX precursor structures can potentially allow synthesis of MXene compositions that cannot be easily prepared with currently available MXene precursors. Additionally, we stress that the structural perfection, grain size and stoichiometry of the precursor have a pronounced impact on the structure and properties of the resulting MXene^{55,61}.

Etching–exfoliation and intercalation–delamination mechanisms should also be studied in concert with MXene precursor preparation as (1) the MXene precursor structure and composition affects its etching effectiveness and (2) the T_x functionalities conferred by the etching process directly alter the intercalant–surface–solvent interactions and thus the feasibility of the intercalant delaminating the multi-layered MXene. These processes are most efficiently studied through a combination of theoretical simulations and modelling at different length and time scales^{84,87}, with in situ and ex situ characterization⁸⁶, to track them stepwise. Furthermore, because these processes (that is, etching, exfoliation, intercalation and delamination) are also responsible for creating surface T_x groups that directly influence MXene properties, a mechanistic understanding of these processes may enable intercalation⁹⁸ and T_x -engineered⁷ MXenes with tailored electronic and/or magnetic properties, such as ferromagnetism⁹⁸ or semiconductivity⁷.

We additionally highlight Lewis acid molten salt etching^{37,58,71,79} as a nascent but important synthetic method towards nitride MXenes, and new T_x chemical identities beyond those from conventional solution-based etching^{7,37,58}. This method is particularly relevant for nitride MXenes, which, despite their promising electronic and ferromagnetic properties for spintronics¹⁰⁹, have been synthesized with

limited success^{45,47,74,75} in comparison to carbide MXenes. Therefore, targeted etching and exfoliation work is required for selective M–A bond etching over the M–N bond, which is complicated by the higher predicted M_2AN exfoliation energy to produce nitride MXenes, compared to that of M_2AC to produce carbide MXenes (Fig. 2g)⁴⁰.

It is important to note that the storage and stability of MXenes is an active area of research within the MXene community. Given that both the MAX and MXene synthesis methods strongly influence the resistance to oxidation and hydrolysis of the resultant MXenes (Fig. 3f)^{55,61}, extending our understanding of the etching–exfoliation and intercalation–delamination mechanisms will also help to prevent MXene degradation and produce MXenes with enhanced oxidative and aqueous phase stability¹¹⁰. As previously mentioned, the use of excess Ti and Al in Ti_3AlC_2 synthesis was reported to increase the ambient stability of $Ti_3C_2T_x$ suspended in aqueous solutions from a week to at least 10 months⁵⁵. The increased stability was attributed to increased carbon content in the carbon sublattice of Ti_3AlC_2 when using excess Ti and Al, which reduces Ti surface vacancies and defects in the final structure⁵⁵. Future studies are necessary to elucidate the role of defects and the stoichiometry of the MAX precursors on the quality and stability of the MXene sheets produced from them. Etching and delamination protocols are also important steps to control the quality of MXene through surface terminations, defects and flake size. For example, increasing the HF concentration is known to increase the concentration of defects in the resultant MXene¹¹¹. Thus, instead of adding all the acid at the start of the synthesis, prolonged HF addition to maintain a low HF concentration in the reaction vessel may further improve the quality

of the resultant MXene. These examples demonstrate the need for controlling all synthetic parameters at every step of the process for producing high-quality MXenes.

While MXenes continue to expand into new fields as a consequence of their tunable properties, scalable synthesis, and promising predicted and actual performance, efforts have been undertaken to enable high-throughput and scalable MAX⁷⁷ and MXene^{22,25} (top-down) manufacturing. Ti₃AlC and Ti₃AlC₂ are both produced commercially in hundreds of kilograms, although synthesis from low-cost precursors is essential for further adoption of these materials¹¹². Additionally, Ti₃C₂T_x has been successfully produced in large quantities as films (1-m long, 10-cm wide, 940-nm thick) through blade coating²², powders (50 g per batch)²⁵ and colloidal suspensions (5 l of 10 mg ml⁻¹ per batch) through HF etching in batch reactors²⁵. This large-scale processability of MXenes is a considerable advantage over many other 2D materials that are produced by bottom-up approaches in small quantities. Additionally, no notable differences in the chemical and physical properties were observed when producing Ti₃C₂T_x at the 1-g or 50-g batch scale²⁵. When scaling MXene HF etching from the laboratory bench to larger scales, deliberate attention should be paid to the monitoring (using probes), processing (homogeneous mixing and agitation) and control of reaction conditions (temperature, pH) and by-products (H₂ gas)²⁵.

On environmental, health and sustainability fronts, engineering controls should be put in place to minimize or eliminate HF exposure and prevent thermal runaway caused by exothermic reactions during the initial mixing of MXene precursors with the etchant^{43,25}. Although other MXenes are expected to be similarly scalable synthetically through HF etching, the practical viability of scaling HF etching to produce MXenes beyond Ti₃C₂T_x should be evaluated, given that each MXene etches at a different HF concentration and temperature¹¹. We anticipate that the development of scalable Lewis acid molten salt etching^{37,58,71,79} will be highly complementary by producing MXenes that cannot be presently made through HF etching, such as nitride MXenes and MXenes with new T_x groups, hence opening future opportunities.

Received: 18 October 2021; Accepted: 23 May 2022;

Published online: 1 August 2022

References

- Naguib, M. et al. Two-dimensional nanocrystals produced by exfoliation of Ti₃AlC₂. *Adv. Mater.* **23**, 4248–4253 (2011).
- Gogotsi, Y. & Anasori, B. The rise of MXenes. *ACS Nano* **13**, 8491–8494 (2019).
- VahidMohammadi, A., Rosen, J. & Gogotsi, Y. The world of two-dimensional carbides and nitrides (MXenes). *Science* **372**, eabf1581 (2021).
- Gogotsi, Y. & Huang, Q. MXenes: two-dimensional building blocks for future materials and devices. *ACS Nano* **15**, 5775–5780 (2021).
- Shayesteh Zeraati, A. et al. Improved synthesis of Ti₃C₂T_x MXenes resulting in exceptional electrical conductivity, high synthesis yield and enhanced capacitance. *Nanoscale* **13**, 3572–3580 (2021).
- Abdolhosseinzadeh, S., Jiang, X., Zhang, H., Qiu, J. & Zhang, C. Perspectives on solution processing of two-dimensional MXenes. *Mater. Today* **48**, 214–240 (2021).
- Kamysbayev, V. et al. Covalent surface modifications and superconductivity of two-dimensional metal carbide MXenes. *Science* **369**, 979–983 (2020).
- Lipatov, A. et al. Electrical and elastic properties of individual single-layer Nb₄C₃T_x MXene flakes. *Adv. Electron. Mater.* **6**, 1901382 (2020).
- Lim, K. R. G. et al. Rational design of two-dimensional transition metal Carbide/Nitride (MXene) hybrids and nanocomposites for catalytic energy storage and conversion. *ACS Nano* **14**, 10834–10864 (2020).
- Saravanan, P., Rajeswari, S., Kumar, J. A., Rajasimman, M. & Rajamohan, N. Bibliometric analysis and recent trends on MXene research—a comprehensive review. *Chemosphere* **286**, 131873 (2022).
- Wei, Y., Zhang, P., Soomro, R. A., Zhu, Q. & Xu, B. Advances in the synthesis of 2D MXenes. *Adv. Mater.* **33**, 2103148 (2021).
- Anasori, B. & Gogotsi, Y. (eds) *2D Metal Carbides and Nitrides (MXenes): Structure, Properties and Applications* (Springer, 2019); <https://doi.org/10.1007/978-3-030-19026-2>
- Wyatt, B. C., Rosenkranz, A. & Anasori, B. 2D MXenes: tunable mechanical and tribological properties. *Adv. Mater.* **33**, 2007973 (2021).
- Hope, M. A. et al. NMR reveals the surface functionalisation of Ti₃C₂ MXene. *Phys. Chem. Chem. Phys.* **18**, 5099–5102 (2016).
- Mashtalir, O. et al. Intercalation and delamination of layered carbides and carbonitrides. *Nat. Commun.* **4**, 1716 (2013).
- Naguib, M., Unocic, R. R., Armstrong, B. L. & Nanda, J. Large-scale delamination of multi-layers transition metal carbides and carbonitrides 'MXenes'. *Dalton Trans.* **44**, 9353–9358 (2015).
- Anasori, B. et al. Two-dimensional, ordered, double transition metals carbides (MXenes). *ACS Nano* **9**, 9507–9516 (2015).
- Nemani, S. K. et al. High-entropy 2D carbide MXenes: TiVnNbMoC₃ and TiVCrMoC₃. *ACS Nano* **15**, 12815–12825 (2021).
- Zhou, J. et al. High-entropy laminate metal carbide (MAX Phase) and its two-dimensional derivative MXene. *Chem. Mater.* **34**, 2098–2106 (2022).
- Naguib, M., Barsoum, M. W. & Gogotsi, Y. Ten years of progress in the synthesis and development of MXenes. *Adv. Mater.* **33**, 2103393 (2021).
- Alhabeib, M. et al. Guidelines for synthesis and processing of two-dimensional titanium carbide (Ti₃C₂T_x MXene). *Chem. Mater.* **29**, 7633–7644 (2017).
- Zhang, J. et al. Scalable manufacturing of free-standing, strong Ti₃C₂T_x MXene films with outstanding conductivity. *Adv. Mater.* **32**, 2001093 (2020).
- Shuck, C. E. et al. Safe synthesis of MAX and MXene: guidelines to reduce risk during synthesis. *ACS Chem. Health Saf.* **28**, 326–338 (2021).
- Verger, L., Natu, V., Carey, M. & Barsoum, M. W. MXenes: an introduction of their synthesis, select properties and applications. *Trends Chem.* **1**, 656–669 (2019).
- Shuck, C. E. et al. Scalable synthesis of Ti₃C₂T_x MXene. *Adv. Eng. Mater.* **22**, 1901241 (2020).
- Xu, C. et al. Large-area high-quality 2D ultrathin Mo₂C superconducting crystals. *Nat. Mater.* **14**, 1135–1141 (2015).
- Fan, Y. et al. Recent advances in growth of transition metal carbides and nitrides (MXenes) crystals. *Adv. Funct. Mater.* **32**, 2111357 (2022).
- Oyama, S. T. (ed.) *The Chemistry of Transition Metal Carbides and Nitrides* (Springer, 1996); <https://doi.org/10.1007/978-94-009-1565-7>
- Oyama, S. T. Preparation and catalytic properties of transition metal carbides and nitrides. *Catal. Today* **15**, 179–200 (1992).
- Wuchina, E., Opila, E., Opeka, M., Fahrenholtz, B. & Talmy, I. UHTCs: ultra-high temperature ceramic materials for extreme environment applications. *Electrochem. Soc. Interface* **16**, 30–36 (2007).
- Han, M. et al. Tailoring electronic and optical properties of MXenes through forming solid solutions. *J. Am. Chem. Soc.* **142**, 19110–19118 (2020).
- Hantanasisirakul, K. et al. Evidence of a magnetic transition in atomically thin Cr₂TiC₂T_x MXene. *Nanoscale Horiz.* **5**, 1557–1565 (2020).
- Zhou, J. et al. Synthesis and electrochemical properties of two-dimensional hafnium carbide. *ACS Nano* **11**, 3841–3850 (2017).
- Tao, Q. et al. Two-dimensional Mo_{1.33}C MXene with divacancy ordering prepared from parent 3D laminate with in-plane chemical ordering. *Nat. Commun.* **8**, 14949 (2017).
- Hong, W., Wyatt, B. C., Nemani, S. K. & Anasori, B. Double transition-metal MXenes: atomistic design of two-dimensional carbides and nitrides. *MRS Bull.* **45**, 850–861 (2020).
- Sokol, M., Natu, V., Kota, S. & Barsoum, M. W. On the chemical diversity of the MAX phases. *Trends Chem.* **1**, 210–223 (2019).
- Li, Y. et al. A general Lewis acidic etching route for preparing MXenes with enhanced electrochemical performance in non-aqueous electrolyte. *Nat. Mater.* **19**, 894–899 (2019).
- Weidman, M. C., Esposito, D. V., Hsu, Y.-C. & Chen, J. G. Comparison of electrochemical stability of transition metal carbides (WC, W₂C, Mo₂C) over a wide pH range. *J. Power Sources* **202**, 11–17 (2012).
- Mikeska, K. R., Bennison, S. J. & Grise, S. L. Corrosion of ceramics in aqueous hydrofluoric acid. *J. Am. Ceram. Soc.* **83**, 1160–1164 (2004).
- Khaledialidusti, R., Khazaei, M., Khazaei, S. & Ohno, K. High-throughput computational discovery of ternary-layered MAX phases and prediction of their exfoliation for formation of 2D MXenes. *Nanoscale* **13**, 7294–7307 (2021).
- Gkoutaras, A. et al. Mechanical exfoliation of select MAX Phases and Mo₃Ce₄Al₃ single crystals to produce MAXenes. *Small* **16**, 1905784 (2020).
- Dahlqvist, M. & Rosen, J. Predictive theoretical screening of phase stability for chemical order and disorder in quaternary 312 and 413 MAX phases. *Nanoscale* **12**, 785–794 (2020).
- Dahlqvist, M., Petruhins, A., Lu, J., Hultman, L. & Rosen, J. Origin of chemically ordered atomic laminates (*i*-MAX): expanding the elemental space by a theoretical/experimental approach. *ACS Nano* **12**, 7761–7770 (2018).
- Khazaei, M. et al. Insights into exfoliation possibility of MAX phases to MXenes. *Phys. Chem. Chem. Phys.* **20**, 8579–8592 (2018).

45. Urbankowski, P. et al. Synthesis of two-dimensional titanium nitride Ti_4N_3 (MXene). *Nanoscale* **8**, 11385–11391 (2016).
46. Magnuson, M. & Mattesini, M. Chemical bonding and electronic-structure in MAX phases as viewed by X-ray spectroscopy and density functional theory. *Thin Solid Films* **621**, 108–130 (2017).
47. Johnson, D., Qiao, Z., Uwadiunor, E. & Djire, A. Holdups in Nitride MXene's development and limitations in advancing the field of MXene. *Small* **18**, 2106129 (2022).
48. Han, M. et al. Beyond $Ti_3C_2T_x$: MXenes for electromagnetic interference shielding. *ACS Nano* **14**, 5008–5016 (2020).
49. Alhabeib, M. et al. Selective etching of silicon from Ti_3SiC_2 (MAX) to obtain 2D titanium carbide (MXene). *Angew. Chem. Int. Ed.* **57**, 5444–5448 (2018).
50. Meshkian, R. et al. Synthesis of two-dimensional molybdenum carbide, Mo_2C , from the gallium based atomic laminate Mo_2Ga_2C . *Scr. Mater.* **108**, 147–150 (2015).
51. Halim, J. et al. Synthesis and characterization of 2D molybdenum carbide (MXene). *Adv. Funct. Mater.* **26**, 3118–3127 (2016).
52. Lapauw, T. et al. Synthesis of MAX phases in the Hf-Al-C system. *Inorg. Chem.* **55**, 10922–10927 (2016).
53. Sun, Z., Zou, Y., Tada, S. & Hashimoto, H. Effect of Al addition on pressureless reactive sintering of Ti_3SiC_2 . *Scr. Mater.* **55**, 1011–1014 (2006).
54. Perevislov, S. N., Sokolova, T. V. & Stolyarova, V. L. The Ti_3SiC_2 MAX phases as promising materials for high temperature applications: formation under various synthesis conditions. *Mater. Chem. Phys.* **267**, 124625 (2021).
55. Mathis, T. S. et al. Modified MAX phase synthesis for environmentally stable and highly conductive Ti_3C_2 MXene. *ACS Nano* **15**, 6420–6429 (2021).
56. Naguib, M. et al. Two-dimensional transition metal carbides. *ACS Nano* **6**, 1322–1331 (2012).
57. Chen, W. et al. Synthesis and formation mechanism of high-purity Ti_3AlC_2 powders by microwave sintering. *Int. J. Appl. Ceram. Technol.* **17**, 778–789 (2020).
58. Li, M. et al. Element replacement approach by reaction with Lewis acidic molten salts to synthesize nanolaminated MAX phases and MXenes. *J. Am. Chem. Soc.* **141**, 4730–4737 (2019).
59. Sychev, A. E., Busurina, M. L., Sachkova, N. V. & Vrel, D. Interaction of graphite with a Ti-Al melt during self-propagating high-temperature synthesis. *Inorg. Mater.* **55**, 780–784 (2019).
60. Fonseca, A. F. et al. Titanium-carbide formation at defective curved graphene-titanium interfaces. *MRS Adv.* **3**, 457–462 (2018).
61. Shuck, C. E. et al. Effect of Ti_3AlC_2 MAX phase on structure and properties of resultant $Ti_3C_2T_x$ MXene. *ACS Appl. Nano Mater.* **2**, 3368–3376 (2019).
62. Riley, D. P. & Kisi, E. H. The design of crystalline precursors for the synthesis of $M_{n-1}AX_n$ phases and their application to Ti_3AlC_2 . *J. Am. Ceram. Soc.* **90**, 2231–2235 (2007).
63. Sarycheva, A. et al. 2D titanium carbide (MXene) for wireless communication. *Sci. Adv.* **4**, eaau0920 (2018).
64. Verger, L. et al. Overview of the synthesis of MXenes and other ultrathin 2D transition metal carbides and nitrides. *Curr. Opin. Solid State Mater. Sci.* **23**, 149–163 (2019).
65. Li, T. et al. Fluorine-free synthesis of high-purity $Ti_3C_2T_x$ ($T=OH, O$) via alkali treatment. *Angew. Chem. Int. Ed.* **57**, 6115–6119 (2018).
66. Chen, H., Ma, H. & Li, C. Host-guest intercalation chemistry in MXenes and its implications for practical applications. *ACS Nano* **15**, 15502–15537 (2021).
67. Yang, S. et al. Fluoride-free synthesis of two-dimensional titanium carbide (MXene) using a binary aqueous system. *Angew. Chem. Int. Ed.* **57**, 15491–15495 (2018).
68. Pang, S.-Y. et al. Universal strategy for HF-free facile and rapid synthesis of two-dimensional MXenes as multifunctional energy materials. *J. Am. Chem. Soc.* **141**, 9610–9616 (2019).
69. Jawaid, A. et al. Halogen etch of Ti_3AlC_2 MAX phase for MXene fabrication. *ACS Nano* **15**, 2771–2777 (2021).
70. Shi, H. et al. Ambient-stable two-dimensional titanium carbide (MXene) enabled by iodine etching. *Angew. Chem. Int. Ed.* **60**, 8689–8693 (2021).
71. Shen, M. et al. One-pot green process to synthesize MXene with controllable surface terminations using molten salts. *Angew. Chem. Int. Ed.* **60**, 27013–27018 (2021).
72. Sun, Z. et al. Selective lithiation-expansion-microexplosion synthesis of two-dimensional fluoride-free MXene. *ACS Mater. Lett.* **1**, 628–632 (2019).
73. Natu, V. et al. 2D $Ti_3C_2T_x$ MXene synthesized by water-free etching of Ti_3AlC_2 in polar organic solvents. *Chem* **6**, 616–630 (2020).
74. Soundiraraju, B. & George, B. K. Two-dimensional titanium nitride (Ti_2N) MXene: synthesis, characterization, and potential application as surface-enhanced Raman scattering substrate. *ACS Nano* **11**, 8892–8900 (2017).
75. Djire, A., Zhang, H., Liu, J., Miller, E. M. & Neale, N. R. Electrocatalytic and optoelectronic characteristics of the two-dimensional titanium nitride $Ti_4N_3T_x$ MXene. *ACS Appl. Mater. Interfaces* **11**, 11812–11823 (2019).
76. Chen, J. et al. Molten salt shielded synthesis (MS^3) of MXene in air. *Energy Environ. Mater.* <https://doi.org/10.1002/eem2.12328> (2021).
77. Bärmann, P. et al. Scalable synthesis of MAX phase precursors toward titanium-based MXenes for lithium-ion batteries. *ACS Appl. Mater. Interfaces* **13**, 26074–26083 (2021).
78. Ma, G. et al. Li-ion storage properties of two-dimensional titanium-carbide synthesized via fast one-pot method in air atmosphere. *Nat. Commun.* **12**, 5085 (2021).
79. Liu, L. et al. Exfoliation and delamination of $Ti_3C_2T_x$ MXene prepared via molten salt etching route. *ACS Nano* **16**, 111–118 (2022).
80. Seredych, M. et al. High-temperature behavior and surface chemistry of carbide MXenes studied by thermal analysis. *Chem. Mater.* **31**, 3324–3332 (2019).
81. Lu, J. et al. $Ti_{n+1}C_n$ MXenes with fully saturated and thermally stable Cl terminations. *Nanoscale Adv.* **1**, 3680–3685 (2019).
82. Lee, J. T. et al. Covalent surface modification of $Ti_3C_2T_x$ MXene with chemically active polymeric ligands producing highly conductive and ordered microstructure films. *ACS Nano* **15**, 19600–19612 (2021).
83. Lukatskaya, M. R. et al. Cation intercalation and high volumetric capacitance of two-dimensional titanium carbide. *Science* **341**, 1502–1505 (2013).
84. Srivastava, P., Mishra, A., Mizuseki, H., Lee, K.-R. & Singh, A. K. Mechanistic insight into the chemical exfoliation and functionalization of Ti_3C_2 MXene. *ACS Appl. Mater. Interfaces* **8**, 24256–24264 (2016).
85. Ibragimova, R., Erhart, P., Rinke, P. & Komsa, H.-P. Surface functionalization of 2D MXenes: trends in distribution, composition and electronic properties. *J. Phys. Chem. Lett.* **12**, 2377–2384 (2021).
86. Kim, Y.-J. et al. Etching mechanism of monoatomic aluminum layers during MXene synthesis. *Chem. Mater.* **33**, 6346–6355 (2021).
87. Kim, Y. et al. Elementary processes governing V_2AlC chemical etching in HF. *RSC Adv.* **10**, 25266–25274 (2020).
88. Mashtalir, O., Naguib, M., Dyatkin, B., Gogotsi, Y. & Barsoum, M. W. Kinetics of aluminum extraction from Ti_3AlC_2 in hydrofluoric acid. *Mater. Chem. Phys.* **139**, 147–152 (2013).
89. Meng, F. et al. MXene sorbents for removal of urea from dialysate: a step toward the wearable artificial kidney. *ACS Nano* **12**, 10518–10528 (2018).
90. Li, Y., Huang, S., Wei, C., Wu, C. & Mochalin, V. N. Adhesion of two-dimensional titanium carbides (MXenes) and graphene to silicon. *Nat. Commun.* **10**, 3014 (2019).
91. Zhou, X., Guo, Y., Wang, D. & Xu, Q. Nano friction and adhesion properties on Ti_3C_2 and Nb_2C MXene studied by AFM. *Tribol. Int.* **153**, 106646 (2021).
92. Maleski, K., Mochalin, V. N. & Gogotsi, Y. Dispersions of two-dimensional titanium carbide MXene in organic solvents. *Chem. Mater.* **29**, 1632–1640 (2017).
93. Kim, D. et al. Nonpolar organic dispersion of 2D $Ti_3C_2T_x$ MXene flakes via simultaneous interfacial chemical grafting and phase transfer method. *ACS Nano* **13**, 13818–13828 (2019).
94. Voigt, C. A., Ghidui, M., Natu, V. & Barsoum, M. W. Anion adsorption, $Ti_3C_2T_x$ MXene multilayers, and their effect on claylike swelling. *J. Phys. Chem. C* **122**, 23172–23179 (2018).
95. Kajiyama, S. et al. Enhanced Li-ion accessibility in MXene titanium carbide by steric chloride termination. *Adv. Energy Mater.* **7**, 1601873 (2017).
96. Natu, V. et al. Effect of base/nucleophile treatment on interlayer ion intercalation, surface terminations, and osmotic swelling of $Ti_3C_2T_x$ MXene multilayers. *Chem. Mater.* **34**, 678–693 (2022).
97. Zhao, X. et al. pH, nanosheet concentration and antioxidant affect the oxidation of $Ti_3C_2T_x$ and Ti_2CT_x MXene dispersions. *Adv. Mater. Interfaces* **7**, 2000845 (2020).
98. Hart, J. L. et al. Control of MXenes' electronic properties through termination and intercalation. *Nat. Commun.* **10**, 522 (2019).
99. Shpigel, N. et al. Direct assessment of nanoconfined water in 2D Ti_3C_2 electrode interspaces by a surface acoustic technique. *J. Am. Chem. Soc.* **140**, 8910–8917 (2018).
100. Gao, Q. et al. Tracking ion intercalation into layered Ti_3C_2 MXene films across length scales. *Energy Environ. Sci.* **13**, 2549–2558 (2020).
101. Chen, H. et al. Pristine titanium carbide MXene films with environmentally stable conductivity and superior mechanical strength. *Adv. Funct. Mater.* **30**, 1906996 (2020).
102. Deng, Y. et al. Fast gelation of $Ti_3C_2T_x$ MXene initiated by metal ions. *Adv. Mater.* **31**, 1902432 (2019).
103. Chen, H. et al. Pristine titanium carbide MXene hydrogel matrix. *ACS Nano* **14**, 10471–10479 (2020).
104. Ghidui, M., Lukatskaya, M. R., Zhao, M.-Q., Gogotsi, Y. & Barsoum, M. W. Conductive two-dimensional titanium carbide 'clay' with high volumetric capacitance. *Nature* **516**, 78–81 (2014).
105. Zhang, J. et al. Single platinum atoms immobilized on an MXene as an efficient catalyst for the hydrogen evolution reaction. *Nat. Catal.* **1**, 985–992 (2018).
106. Li, G. et al. 2D titanium carbide (MXene) based films: expanding the frontier of functional film materials. *Adv. Funct. Mater.* **31**, 2105043 (2021).

107. Li, Y. et al. Multielemental single-atom-thick A layers in nanolaminated $V_2(\text{Sn}, A)\text{C}$ ($A = \text{Fe}, \text{Co}, \text{Ni}, \text{Mn}$) for tailoring magnetic properties. *Proc. Natl Acad. Sci. USA* **117**, 820–825 (2020).
108. Jakubczak, M., Szuplewska, A., Rozmysłowska-Wojciechowska, A., Rosenkranz, A. & Jastrzębska, A. M. Novel 2D MBenes—synthesis, structure and biotechnological potential. *Adv. Funct. Mater.* **31**, 2103048 (2021).
109. Kumar, H. et al. Tunable magnetism and transport properties in nitride MXenes. *ACS Nano* **11**, 7648–7655 (2017).
110. Cao, F. et al. Recent advances in oxidation stable chemistry of 2D MXenes. *Adv. Mater.* **34**, 2107554 (2022).
111. Cui, W., Hu, Z.-Y., Unocic, R. R., Van Tendeloo, G. & Sang, X. Atomic defects, functional groups and properties in MXenes. *Chin. Chem. Lett.* **32**, 339–344 (2021).
112. Jolly, S., Paranthaman, M. P. & Naguib, M. Synthesis of $\text{Ti}_3\text{C}_2\text{T}_z$ MXene from low-cost and environmentally friendly precursors. *Mater. Today Adv.* **10**, 100139 (2021).
113. Seh, Z. W. et al. Two-dimensional molybdenum carbide (MXene) as an efficient electrocatalyst for hydrogen evolution. *ACS Energy Lett.* **1**, 589–594 (2016).
114. Shahzad, F. et al. Electromagnetic interference shielding with 2D transition metal carbides (MXenes). *Science* **353**, 1137–1140 (2016).
115. Bhardwaj, R. & Hazra, A. MXene-based gas sensors. *J. Mater. Chem. C* **9**, 15735–15754 (2021).
116. Zamhuri, A., Lim, G. P., Ma, N. L., Tee, K. S. & Soon, C. F. MXene in the lens of biomedical engineering: synthesis, applications and future outlook. *Biomed. Eng. Online* **20**, 33 (2021).
117. Song, M., Pang, S., Guo, F., Wong, M. & Hao, J. Fluoride-free 2D niobium carbide MXenes as stable and biocompatible nanoplatforms for electrochemical biosensors with ultrahigh sensitivity. *Adv. Sci.* **7**, 2001546 (2020).
118. Xuan, J. et al. Organic-base-driven intercalation and delamination for the production of functionalized titanium carbide nanosheets with superior photothermal therapeutic performance. *Angew. Chem. Int. Ed.* **55**, 14569–14574 (2016).
119. Halim, J. et al. Transparent conductive two-dimensional titanium carbide epitaxial thin films. *Chem. Mater.* **26**, 2374–2381 (2014).
120. Hantanasirisakul, K. et al. Effects of synthesis and processing on optoelectronic properties of titanium carbonitride MXene. *Chem. Mater.* **31**, 2941–2951 (2019).
121. Maleski, K., Shuck, C. E., Fafarman, A. T. & Gogotsi, Y. The broad chromatic range of two-dimensional transition metal carbides. *Adv. Opt. Mater.* **9**, 2001563 (2021).
122. Anasori, B. et al. Control of electronic properties of 2D carbides (MXenes) by manipulating their transition metal layers. *Nanoscale Horiz.* **1**, 227–234 (2016).

Acknowledgements

K.R.G.L. acknowledges financial support from the Agency for Science, Technology and Research (A*STAR) Singapore National Science Scholarship (PhD). B.C.W. acknowledges financial support from the National Defense Engineering & Science Graduate Fellowship Program. M.S. acknowledges financial support from Murata Manufacturing, Japan. B.A. acknowledges funding from the US National Science Foundation (grant no. CMMI-2134607). Y.G. acknowledges funding from the US National Science Foundation (grant no. DMR-2041050). Z.W.S. acknowledges the support of the Singapore National Research Foundation (NRF-NRFF2017-04) and Agency for Science, Technology and Research (Central Research Fund Award).

Author contributions

K.R.G.L., M.S. and B.C.W. conducted the literature review and wrote the manuscript under the supervision of B.A., Y.G. and Z.W.S. All authors have given approval to the final version of the manuscript.

Competing interests

The authors declare no competing interests.

Additional information

Supplementary information The online version contains supplementary material available at <https://doi.org/10.1038/s44160-022-00104-6>.

Correspondence should be addressed to Babak Anasori, Yury Gogotsi or Zhi Wei Seh.

Peer review information *Nature Synthesis* thanks Qing Huang and the other, anonymous, reviewer(s) for their contribution to the peer review of this work. Primary Handling Editor: Alison Stoddart, in collaboration with the *Nature Synthesis* team.

Reprints and permissions information is available at www.nature.com/reprints.

Publisher's note Springer Nature remains neutral with regard to jurisdictional claims in published maps and institutional affiliations.

© Springer Nature Limited 2022